

# Strategies for enhancing spin-shuttling fidelities in Si/SiGe quantum wells with random-alloy disorder

Merritt P. Losert,<sup>1,\*</sup> Max Oberländer,<sup>2,\*</sup> Julian D. Teske,<sup>2</sup> Mats Volmer,<sup>2</sup> Lars R. Schreiber,<sup>2,3</sup> Hendrik Bluhm,<sup>2,3,†</sup> S. N. Coppersmith,<sup>4</sup> and Mark Friesen<sup>1,‡</sup>

<sup>1</sup>*Department of Physics, University of Wisconsin-Madison, Madison, Wisconsin 53706, USA*

<sup>2</sup>*JARA-FIT Institute for Quantum Information, Forschungszentrum Jülich GmbH and RWTH Aachen University, 52074 Aachen, Germany*

<sup>3</sup>*ARQUE Systems GmbH, 52074 Aachen, Germany*

<sup>4</sup>*School of Physics, University of New South Wales, Sydney, New South Wales 2052, Australia*

(Dated: May 24, 2024)

Coherent coupling between distant qubits is needed for any scalable quantum computing scheme. In quantum dot systems, one proposal for long-distance coupling is to coherently transfer electron spins across a chip in a moving dot potential. Here, we use simulations to study challenges for spin shuttling in Si/SiGe heterostructures caused by the valley degree of freedom. We show that for devices with valley splitting dominated by alloy disorder, one can expect to encounter pockets of low valley splitting, given a long-enough shuttling path. At such locations, inter-valley tunneling leads to dephasing of the spin wavefunction, substantially reducing the shuttling fidelity. We show how to mitigate this problem by modifying the heterostructure composition, or by varying the vertical electric field, the shuttling velocity, the shape and size of the dot, or the shuttling path. We further show that combinations of these strategies can reduce the shuttling infidelity by several orders of magnitude, putting shuttling fidelities sufficient for error correction within reach.

## I. INTRODUCTION

Quantum dots formed in Si/SiGe heterostructures are a promising technology for scalable quantum computing. Their strengths include the fact that silicon and germanium both have abundant zero-spin isotopes and are compatible with existing semiconductor fabrication technologies. Moreover, one- and two-qubit gate fidelities in Si/SiGe have now exceeded 99% [1–3]. However, scalable quantum computing also requires the coupling of distant qubits, which is not possible via short-ranged exchange interactions. Coupling qubits beyond the nearest neighbor is therefore a topic of great current interest [4–12]. Among other approaches [8, 13, 14], one promising strategy consists of physically shuttling the qubits over distances of one or more microns [15–26].

Two main shuttling schemes have been proposed for quantum dot qubits: the *bucket-brigade* mode and the *conveyor* mode. In the bucket-brigade mode, the electron is moved serially along a line of quantum dots, by modulating the detuning potential between nearest neighbors [16, 24]. In the conveyor mode, which is the topic of this work, phase-shifted sinusoidal potentials are applied to interleaved clavier gates along a channel defined by two screening gates, yielding a moving potential well that carries the electron across a device [24]. A schematic illustration of a conveyor-mode device is shown in Figs. 1(a) and 1(b).

Experimentally, high-fidelity charge shuttling of electrons has now been demonstrated in silicon over distances

of  $\sim 20\ \mu\text{m}$  [16, 19, 26], while phase-coherent shuttling has been demonstrated over distances of  $\sim 400\ \text{nm}$  [25]. Other experiments have demonstrated transfer across a double dot [20], and repeated transport of spins, without spin flips, through a short dot array [23]. However, an important question remains: what are the dominant limitations to coherent spin transfer over extended distances?

One of the main challenges for Si/SiGe qubits, which also affects spin shuttling, is the near-degeneracy of the two low-lying valley states [27, 28]. The energy spacing between these states, known as the valley splitting, can be as large as  $300\ \mu\text{eV}$  in some cases, but can also be lower than  $30\ \mu\text{eV}$  [29–39]. Recent theoretical advancements have shown that, for current state-of-the-art heterostructures, random-alloy disorder in the quantum well barriers is the source of the wide valley-splitting variability [40–43]. Crucially, large valley-splitting fluctuations are even observed in neighboring dots formed on the same chip [41, 44, 45]. These fluctuations inevitably lead to local regions with relatively low valley splittings [46]. While a stationary spin qubit can potentially be shifted away from such a region [30, 33, 47], such fluctuations pose a greater challenge for spin shuttling experiments, where a quantum dot is rapidly shuttled across an extended and highly variable valley-splitting landscape.

Previous theoretical work has considered both the bucket-brigade and conveyor modes of shuttling [24, 48–51]. Detailed models have been employed to study spin transfer; however at present, an extensive analysis of valley-splitting variations is still lacking for realistic heterostructures. In the current work, we incorporate a realistic statistical description of valley-splitting variations caused by alloy disorder, and we apply this to a conveyor-mode shuttling process. In particular, we ap-

\* These two authors contributed equally to this work.

† bluhm@physik.rwth-aachen.de

‡ friesen@physics.wisc.edu

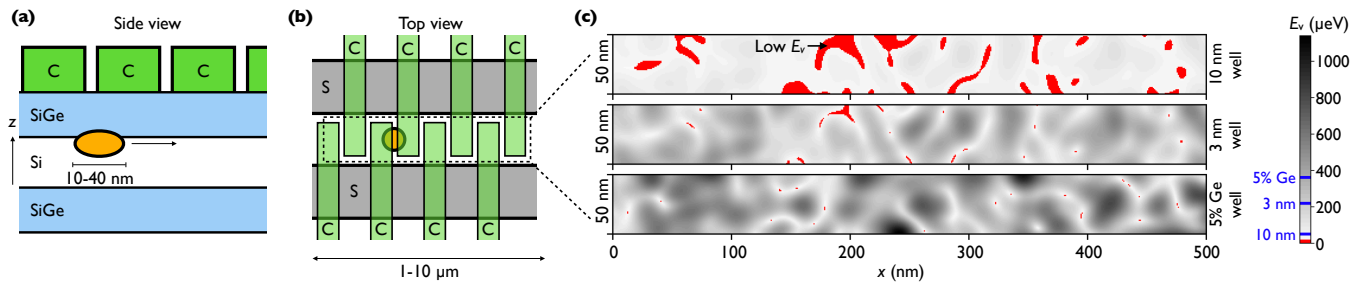


FIG. 1. Schematic illustration of a conveyor-mode spin-shuttling device: (a) side view; (b) top view. A quantum dot in a Si quantum well is confined vertically by the SiGe barriers, and laterally by the electrostatic potential from screening gates (S) and stacked clavier (C) gates. Phase-shifted sinusoidal ac fields are applied to the C gates, yielding a moving potential minimum that carries the electron across the device [24]. (c) Simulated valley-splitting landscapes (top view), as described in Sec. III B, for quantum wells of width 10 nm (top) or 3 nm (middle), and a 10 nm quantum well with a uniform 5% concentration of Ge (bottom). Results are shown for a  $500 \times 50 \text{ nm}^2$  shuttling channel, where “dangerous” regions with  $E_v \leq 20 \mu\text{eV}$  are highlighted in red. We also indicate the average valley splittings for these three quantum wells on the colorbar.

ply the valley-splitting theory derived in Refs. [40, 41] to an effective dynamical model that captures the relevant effects in the parameter regime of interest. Our results show that large valley-splitting variations can cause leakage to the excited valley state, posing a significant challenge for conveyor-mode shuttling architectures where the valley splitting is dominated by alloy disorder. To address this problem, we consider variations of the conventional quantum-well heterostructure that reduce the size of regions with low valley splitting. We also propose and investigate several control strategies to suppress valley-state excitations. By combining these strategies, we show that shuttling fidelities can be improved by several orders of magnitude, enabling high-fidelity shuttling over distances of 10  $\mu\text{m}$ .

The paper is organized as follows. In Sec. II, we provide an intuitive explanation for the dangers of low valley splitting in shuttling experiments. In Sec. III, we review the theory of valley splitting in the presence of alloy disorder. Section IV describes the numerical model we use to simulate spin shuttling, and outlines possible tuning strategies that mitigate the effects of valley excitations. In Sec. V, we describe the results of shuttling simulations across a 10  $\mu\text{m}$  device, while employing different mitigation strategies. In Sec. VI, we comment on the potential scalability of these schemes. Finally in Sec. VII, we summarize our findings and discuss future paths for spin shuttling. Additional details are provided in the Appendices.

## II. EFFECTS OF VALLEY LEAKAGE ON SPIN SHUTTling

In this section, we outline the problems caused by small valley splittings in spin shuttling experiments, leaving mathematical and computational details for later sections. The main problem is leakage outside the computational subspace caused by Landau-Zener transitions

from the valley ground state to the valley excited state. Since the Landé  $g$  factor differs by a small amount  $\delta g$  for these two states, valley excitations cause undesired spin rotations and dephasing. For example, for an external magnetic field of 0.5-1 T [35, 52], the inter-valley Zeeman energy difference can be of order  $\Delta E_B/h = 10 \text{ MHz}$ , yielding spin rotation errors in about 100 ns. In principle, fast valley relaxation processes could mitigate this problem, as we discuss briefly in a later section. However, without applying special procedures to leverage this effect, it should not significantly improve the shuttling fidelity. In this work, we therefore treat valley excitations as errors.

Recent theoretical work has identified two valley-splitting regimes: *disordered* vs *deterministic* [41]. Since deterministically enhanced valley splittings are extremely difficult to achieve in the laboratory, we focus mainly on the disordered case here.

In the disordered regime, valley splitting variability is attributed mainly to alloy disorder, due to the electron overlap with the SiGe alloy. As the Ge exposure increases (for example, by adding Ge to the quantum well), the variability and average value of the valley splitting  $E_v$  also increase. This trend is evident in Fig. 1(c), where we show results of valley-splitting simulations for three different quantum-well profiles, all in the disordered regime. Here in red, we highlight regions where  $E_v < 20 \mu\text{eV}$ , which pose a significant risk for shuttling at speeds of a few meters per second, due to enhanced Landau-Zener tunneling into the excited valley state. (See Appendix C for details.) In the top panel, we consider a conventional quantum well of width 10 nm, and top and bottom interface widths of 1 nm. Here, large portions of the device exhibit dangerously low valley splittings. In the lower two panels, the Ge exposure is further enhanced: the middle panel shows a narrow 3 nm quantum well with 1 nm interfaces, while the lower panel shows a 10 nm quantum well, with a uniform 5% Ge concentration inside the quantum well. As consistent with our expectations, the size of

the dangerous regions decreases in these examples. However, regions of low  $E_v$  still persist. Indeed, as shown in Sec. III B, such regions are *guaranteed* to exist in the disordered regime. For a long-enough shuttling trajectory, a dot is very likely to encounter at least one such region, resulting in valley excitations and subsequent phase errors. In the disordered regime, additional tuning strategies are therefore needed to achieve high shuttling fidelities, as described in Sec. V.

In Sec. V G, we also briefly consider the possibility of valley excitations in the deterministic regime. In this case, the valley splitting can be made uniformly large, with no randomly small values. Inter-valley leakage is then strongly reduced, even in the presence of interfacial disorder, so that high-fidelity spin shuttling is relatively easy to achieve. (See Fig. 6, below, and Appendix A for further details.) However, as noted above, this regime is very difficult to reach experimentally, since it requires the presence of very abrupt features in the quantum-well profile (e.g., super-sharp interfaces, narrower than three atomic monolayers, or 0.4 nm [41]). State-of-the-art growth processes have been shown to produce quantum well interfaces with characteristic widths of 0.8 nm, which do not fall into the deterministic regime [40].

Recent work has therefore suggested alternative strategies for achieving consistently large valley splittings in Si/SiGe systems. For example, shear-strain is known to affect valley splitting in Si systems [53–55], and recent theories have proposed to use shear strain to boost valley splittings in Si/SiGe quantum dots [56]. However, some of these techniques may likewise be challenging to implement in the laboratory. Consequently, we expect the great majority of Si/SiGe devices should fall into the disordered regime, which is more consistent with current fabrication techniques. We therefore focus mainly on the disordered regime in this work.

### III. VALLEY-SPLITTING MODEL

#### A. Effective-mass theory

In this work, we adopt an effective-mass envelope-function formalism to study the valley states, as outlined in Refs. [40, 41]. In this model, the  $\pm z$  valley wavefunctions are approximated by

$$\psi_{\pm}(\mathbf{r}) = e^{\pm ik_0 z} \psi_{\text{env}}(\mathbf{r}), \quad (1)$$

where  $k_0 = 0.82(2\pi/a_0)$  is the position of the valley minimum in the first Brillouin zone and  $a_0 = 0.543$  nm is the size of the conventional Si unit cell. For our purposes, the envelope function  $\psi_{\text{env}}$  is approximately identical for both valleys. The inter-valley coupling matrix element is defined as

$$\Delta = \langle \psi_- | H | \psi_+ \rangle = \int d^3r e^{-2ik_0 z} U_{\text{qw}}(\mathbf{r}) \psi_{\text{env}}^2(\mathbf{r}), \quad (2)$$

where the quantum-well confinement potential  $U_{\text{qw}}$  is the only term in the Hamiltonian  $H$  that significantly couples the two valley states. Since the Ge concentration of the atomic layers along  $\hat{z}$  plays an important role in determining the valley splitting, we may discretize the integral in Eq. (2) as follows:

$$\Delta = \frac{a_0}{4} \sum_l e^{-2ik_0 z_l} U_{\text{qw}}(z_l) |\psi_{\text{env}}(z_l)|^2, \quad (3)$$

where  $l$  is the atomic layer index. The resulting valley splitting is given by  $E_v = 2|\Delta|$ .

The principle observation of Refs. [40, 41] is that alloy disorder partially randomizes  $\Delta$ . We therefore write  $\Delta = \Delta_0 + \delta\Delta$ , where  $\Delta_0$  is the deterministic contribution to  $\Delta$ , and  $\delta\Delta$  arises from random variations of the Ge concentration. To compute these quantities, we define the Si concentration in layer  $l$  as  $X_l$ , where  $X_l$  is averaged over the area of a quantum dot, while the mean concentration  $\bar{X}_l$  is averaged over the whole atomic layer. In Appendix D, we provide more precise definitions of these quantities, and we describe the relation between  $X_l$  and  $U_{\text{qw}}(z_l)$ , where the latter also depends on the dot size and location.

Following Refs. [40, 41], we characterize the statistical properties of  $\Delta$  in terms of the variance of  $\delta\Delta$ , given by

$$\begin{aligned} \sigma_{\Delta}^2 &= \text{Var}[\delta\Delta] \\ &= \frac{1}{\pi a_x a_y} \left[ \frac{a_0^2 \Delta E_c}{8(X_w - X_s)} \right]^2 \sum_l |\psi_{\text{env}}(z_l)|^4 \bar{X}_l (1 - \bar{X}_l). \end{aligned} \quad (4)$$

Here, we assume the dot is in the ground state of a lateral harmonic confinement potential with characteristic level spacings  $\hbar\omega_{x(y)}$  along the principle  $x(y)$  axes, and characteristic length scales  $a_{x(y)} = \sqrt{\hbar/m_t\omega_{x(y)}}$ , where  $m_t = 0.19m_e$  is the transverse effective mass in Si. The quantity  $\Delta E_c$  defines the conduction-band energy offset between the strained quantum well and the strain-relaxed SiGe barriers. While the quantum well is conventionally formed of pure Si, we also consider more general situations where the well is formed of SiGe alloy, with a different composition than the barriers. The variables  $X_w$  and  $X_s$  then indicate the Si concentrations of the quantum well and the SiGe substrate (i.e., the barriers), respectively. Generally,  $\bar{X}_l$  transitions smoothly between  $X_s$  and  $X_w$ , while  $X_l$  deviates slightly from  $\bar{X}_l$  due to local fluctuations within a quantum dot.

From Eq. (3), we note that  $\Delta$  is a complex quantity, which can be decomposed into its real and imaginary components:  $\Delta = \Delta_R + i\Delta_I$ . Under realistic assumptions about quantum-well interface,  $\Delta_R$  and  $\Delta_I$  are well described here as Gaussian random variables, each having a variance of  $\sigma_{\Delta}^2/2$ . As we show in the following section, this property leads to the existence of regions of arbitrarily small  $E_v$ .

Finally we note that Eq. (4) allows us to directly characterize the valley splitting of a given heterostructure as

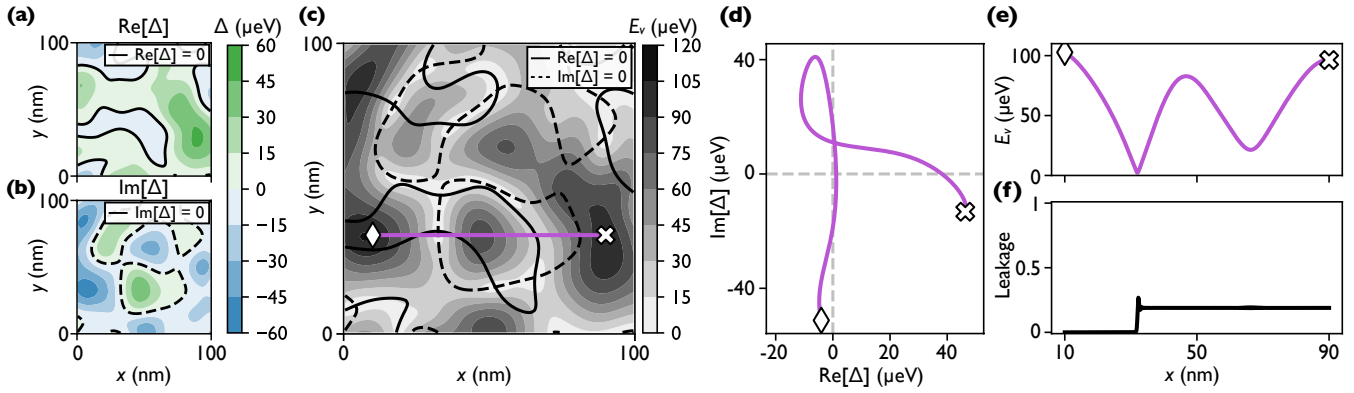


FIG. 2. Points of vanishing valley splitting are topologically guaranteed to occur in the disordered regime. (a),(b) Real and imaginary components of the inter-valley coupling  $\Delta$ , computed across a typical  $100 \times 100 \text{ nm}^2$  region of heterostructure, as described in the main text. Solid and dashed lines highlight contours where  $\text{Re}[\Delta] = 0$  and  $\text{Im}[\Delta] = 0$ , respectively. (c) The valley splitting  $E_v = 2|\Delta|$ , obtained from (a) and (b), with the same contours superimposed. Correlations are observed between these contours and regions with low  $E_v$ . Intersections between the contours correspond to points of vanishing  $E_v$ . A sample path across the heterostructure (purple line) passes nearby one such intersection. (d) The inter-valley coupling  $\Delta$ , and (e) the valley splitting  $E_v$ , along the same path shown in (c). (f) Leakage to the excited valley state caused by Landau-Zener tunneling, simulated for a dot traveling at a velocity of 1 m/s along the same path.

deterministically enhanced vs disordered, based on the crossover between these two regimes, which occurs at  $\sqrt{\pi}\sigma\Delta = 2|\Delta_0|$  [41]. In the deterministic regime, we observe  $|\Delta_0| > |\delta\Delta|$  with high probability, and an average valley splitting of  $\bar{E}_v \approx 2|\Delta_0|$ . (For example, quantum wells with ultra-sharp interfaces exhibit such behavior.) In contrast, in the disordered regime, we find  $|\Delta_0| < |\delta\Delta|$  with high probability, and [41]

$$\bar{E}_v \approx \sqrt{\pi}\sigma\Delta. \quad (5)$$

For conventional heterostructures, like those considered in this work, typical interfaces are not ultra-sharp, and the valley splitting falls into the disordered regime.

### B. Valley-coupling landscape and excitations

As described above, in the disordered regime, the real and imaginary components of  $\Delta$  are independent Gaussian random fields. We now show that this guarantees the existence of regions with arbitrarily small  $E_v$ , scattered across a heterostructure. Figures 2(a) and 2(b) illustrate typical instances of  $\text{Re}[\Delta]$  and  $\text{Im}[\Delta]$  for a  $100 \times 100 \text{ nm}^2$  lateral region of a device. To compute these landscapes, the heterostructure is modeled atomistically by assigning each atom in the crystal lattice as either Si or Ge. The probability of choosing Si at a given lattice site in layer  $l$  is given by  $\bar{X}_l$ . We then perform the one-dimensional (1D) summation in Eq. (3) via the following procedure. First we compute the local Si concentration  $X_l$  by performing the weighted average described in Eq. (D9), for a dot with orbital energies  $\hbar\omega_x = \hbar\omega_y = 2 \text{ meV}$ , centered at  $(x_0, y_0)$ . Next, we use Eq. (D2) to convert the Si concentration profile  $X_l$  to a quantum-well confinement potential  $U_{\text{qw}}(z_l)$ .  $\psi_{\text{env}}(z_l)$  is then computed from

$U_{\text{qw}}(z_l)$  by solving a discretized Schrödinger equation, as described in Appendix D. Equation (3) then gives  $\Delta$  as a function of dot position  $(x_0, y_0)$ , yielding the real and imaginary components shown in Figs. 2(a) and 2(b). The corresponding valley splitting  $E_v = 2|\Delta|$  is plotted in Fig. 2(c).

In Figs. 2(a) and 2(b), we highlight contours where  $\text{Re}[\Delta] = 0$  and  $\text{Im}[\Delta] = 0$ . The same contours are also plotted in Fig. 2(c), where they are seen to correlate with regions of low valley splitting. Points where the contours intersect correspond to zero valley splitting. Importantly, such points are randomly distributed across the heterostructure and are guaranteed to exist in the disordered regime. Their spatial distribution is determined by the dot size, and in the disordered regime, we note that this distribution does not depend on the average valley splitting. Thus, distributions with similar topologies are observed in systems with large average  $E_v$ .

The regions of low valley splitting near  $\Delta \approx 0$  are dangerous for spin shuttling, because the electron can potentially tunnel into the excited valley state via a Landau-Zener process, leading to shuttling errors. This process is illustrated in Figs. 2(c)-2(f). First in Fig. 2(c), we highlight a shuttling path in purple that passes through a region of low  $E_v$ . In Fig. 2(d), the inter-valley coupling  $\Delta$  is plotted along the same path, where it passes very near the origin of the complex plane,  $\Delta = 0$ . The valley splitting,  $E_v = 2|\Delta|$ , is also shown along this path in Fig. 2(e). In Fig. 2(f), we solve the dynamical evolution of the shuttling electron with regards to the two valley states, assuming the valley splitting shown in Fig. 2(e), using the methods described in Sec. IV, below. Specifically, we plot the leakage into the excited valley state, observing a sudden jump near the  $\Delta$  minimum, caused by Landau-Zener tunneling. We expect a similar jump in

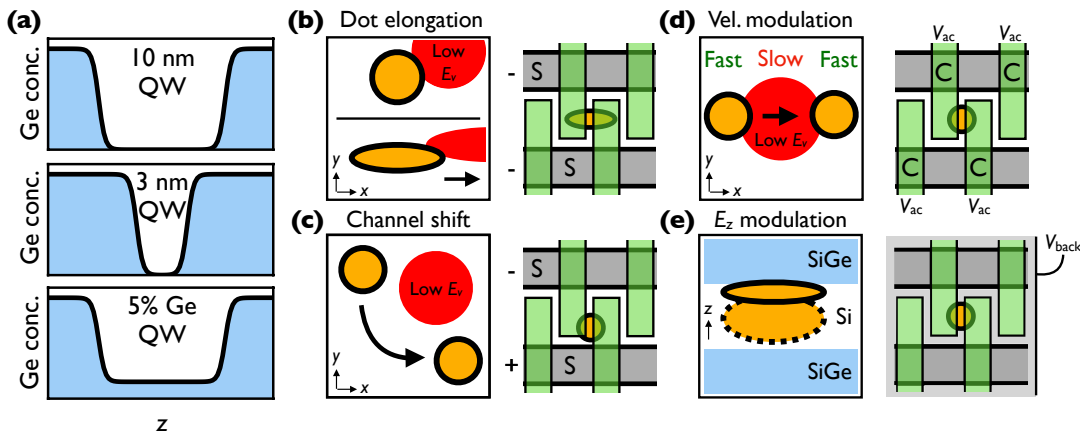


FIG. 3. Overview of the heterostructure tuning strategies considered in this work. (a) Three different quantum wells, including a conventional 10 nm Si quantum well, a narrow 3 nm Si quantum well, and a 10 nm quantum well with a uniform 5% Ge concentration in the middle of the well. (b)-(e) Four strategies proposed for avoiding valley excitations: (b) elongating the dot along the shuttling direction while squeezing the dot in the transverse direction, by applying appropriate voltages to screening gates (S); (c) shifting the position of the dot in the channel to avoid low- $E_v$  regions, by modulating the voltages on S gates; (d) slowing the dot velocity near  $E_v$  minima, by manipulating the ac voltages  $V_{ac}$  applied to the clavier gates (C); (e) modulating the vertical field  $E_z$ , e.g., by introducing a back gate ( $V_{back}$ ).

the shuttling infidelity whenever a shuttling path passes through a region of low valley splitting.

In the above discussion, we have ignored effects like strain fluctuations and valley-orbit interactions that lift the valley-state degeneracy near points of low  $E_v$ . However, these effects are weak, and we expect leakage induced by Landau-Zener processes to remain prevalent in real devices.

Finally, we note that the atomistic method for generating valley-splitting landscapes, described above, is inefficient for determining large-scale statistical properties. To make this process more efficient, we turn instead to a statistical assignment of valley splittings, using the methods described in Appendix E. This assignment makes use of the fact that the real and imaginary components of  $\Delta$  are Gaussian random variables. We note that, to a very good approximation, in the disordered regime, the center of these Gaussian distributions is given by  $|\Delta_0| \approx 0$  [41]. The full statistical description of  $\Delta$  then requires one additional piece of information: the two-point covariance functions for  $\text{Re}[\Delta]$  and  $\text{Im}[\Delta]$ , which were obtained in Ref. [41] as

$$\begin{aligned} \text{Cov}(\text{Re}[\Delta], \text{Re}[\Delta']) &= \text{Cov}(\text{Im}[\Delta], \text{Im}[\Delta']) \\ &= \frac{1}{2} e^{-\delta_x^2/2a_x^2 - \delta_y^2/2a_y^2} \sigma_\Delta^2. \end{aligned} \quad (6)$$

Here,  $\Delta$  and  $\Delta'$  are separated by the spatial vector  $(\delta_x, \delta_y)$  in the  $xy$ -plane. Obtaining valley-coupling landscapes with this method yields results like those shown in Fig. 1(c), which exhibit the correct statistical properties.

## IV. SIMULATING QUANTUM DYNAMICS

### A. Physical device

Figures 1(a) and 1(b) schematically illustrate the devices we consider in this work. During conveyor-mode operation, oscillating voltages are applied to the clavier gates, to produce a moving potential pocket capable of carrying an electron across the device [19]. Unless otherwise specified, we model this potential pocket as an isotropic harmonic confinement potential with orbital splittings  $\hbar\omega_x = \hbar\omega_y = 2 \text{ meV}$ , and we assume the pocket moves with constant speed along the shuttling trajectory. The clavier gates generate a vertical electric field that squeezes the electron against the top quantum-well interface. In some cases, we assume this field can be tuned, for example, by including a back-gate. However, unless otherwise specified, we consider a fixed vertical field of  $E_z = 5 \text{ mV/nm}$ . In Sec. IV C, we consider several additional tuning capabilities that allow us to mitigate the effects of low valley splitting. These include the ability to vary the shuttling velocity, the position of the electron transverse to the shuttling trajectory, and the dot shape (e.g., with  $\omega_x \neq \omega_y$ ). In all cases, we consider a total shuttle length of  $10 \mu\text{m}$ , as consistent with a recent architecture proposal involving a medium-range coupler [22].

We also consider three types of quantum wells, as illustrated in Fig. 3. These include a conventional 10 nm quantum well, and two other wells proposed to give larger average valley splittings: a narrow 3 nm quantum well and a structure containing a uniform 5% Ge concentration inside the quantum well. These are meant to illustrate a range of realistic heterostructures. We model the quantum-well interfaces using sigmoid func-

tions, as described in Appendix D, and assume interface widths of  $\lambda = 1$  nm, unless otherwise specified. (Note that our current goal is not to optimize heterostructure parameters, but to characterize schemes for mitigating the effects of small valley splittings.) As previously noted, the deterministic contribution to the inter-valley coupling can be safely ignored in these heterostructures, with  $\Delta_0 \approx 0$ , since they fall into the disordered regime. The key difference between the heterostructures is therefore their  $\sigma_\Delta$  values, which are related to the average valley splittings through Eq. (5). For the heterostructures described above, we obtain the average values  $\langle E_v(10 \text{ nm}) \rangle \approx 50 \mu\text{eV}$ ,  $\langle E_v(3 \text{ nm}) \rangle \approx 220 \mu\text{eV}$ , and  $\langle E_v(5\%) \rangle \approx 360 \mu\text{eV}$ , respectively. For our dynamical shuttling simulations, we generate many random valley-splitting landscapes, as described in Sec. III B, obtaining results like those shown in Fig. 1 for the three different heterostructures.

## B. Spin-shuttling model

### 1. Hamiltonian

We employ a minimal model to investigate decoherence during shuttling. The model is comprised of two spin and two valley states. In particular, we ignore the presence of orbitally excited states, which relax quickly and are sufficiently separated in energy (1-2 meV) that they play a much smaller role than the valley excited state [24]. Here, we first present the model, then provide discussion of some assumptions built into it. The model is given by

$$H = \frac{E_B}{2} \sigma_z + \mathbf{\Delta}(x) \cdot \boldsymbol{\tau} + \frac{\Delta E_B}{4} [\hat{\mathbf{n}}_\Delta(x) \cdot \boldsymbol{\tau}] \otimes \sigma_z, \quad (7)$$

where  $E_B = g\mu_B B$  is the Zeeman energy,  $g \approx 2$  is the Landé  $g$  factor,  $\mu_B$  is the Bohr magneton,  $B$  is the magnetic field along the spin quantization axis, which does not necessarily coincide with the crystallographic  $z$  axis,  $\Delta E_B = (\delta g)\mu_B B$  is the difference in Zeeman splittings for the two valley states,  $\mathbf{\Delta} = (\Delta_R, \Delta_I)^T$  is the inter-valley coupling (which varies from location to location),  $\hat{\mathbf{n}}_\Delta = \mathbf{\Delta}/|\mathbf{\Delta}|$  denotes the valley quantization axis, and  $\sigma_z$  and  $\boldsymbol{\tau} = (\tau_x, \tau_y)^T$  are Pauli matrices acting on the spin- and valley-spaces, respectively.

Several comments are in order for Eq. (7). First, we note that the  $\Delta E_B$  term ignores any dependence on the magnitude or angular orientation of the magnetic field, as well as local variations of the applied electric field, all of which can affect  $\delta g$ . Moreover, we note that  $\delta g$  also varies slightly by location, due to interface steps and random-alloy disorder [35, 52, 57]. However, we observe almost no dependence of our results on  $\Delta E_B$  (see Appendix F), and we therefore set it here to a fixed value of 10 MHz, reflecting a typical difference in spin-resonance frequencies between the two valley states, as consistent with experimental observations [35, 52].

Second, we note that the model, above, does not include dephasing or relaxation effects, which we now discuss briefly. One relaxation process that could affect shuttling in silicon is the spin-valley hot spot, at which the Zeeman and valley energy splittings are nearly equal, giving rise to fast spin relaxation [33]. An electron could potentially encounter many such hot spots when traversing a wildly varying landscape of valley splittings. We could suppress the effects of these hot spots by shuttling past them as quickly as possible; however, this has other potential pitfalls. A simpler approach is to reduce the number of hot spots by operating at low magnetic fields where the Zeeman splitting is much smaller than the average valley splitting [24]. In this work, we consider low external fields of  $B = 50$  mT [58], which moves the hot spots to below  $10 \mu\text{eV}$ . Although occasional hot spots are still encountered in this regime, Landau-Zener processes are also present, and since they are also detrimental to the shuttling fidelity, it is reasonable to ignore the hot spots in favor of Landau-Zener processes.

Spin dephasing of the shuttling electron occurs over a time scale of  $T_2^*$ , due to the presence of charge or magnetic noise [24]. In Sec. V F, we treat these effects phenomenologically, finding that the presence of both dephasing and leakage suggests that there will be an optimal shuttling speed.

Fast valley relaxation processes present interesting opportunities for solving the valley-state leakage problem, which we will investigate in a future publication. In the present work, we note that experimental measurements of valley relaxation are scarce, but likely of order 10 ms for valley splittings of order  $50 \mu\text{eV}$  [59], which is several orders of magnitude slower than dephasing, and therefore irrelevant. On the other hand, valley lifetimes scale as the inverse-fifth power of the valley splitting [24, 60], so valley and dephasing timescales could become comparable for very large valley splittings of order  $500 \mu\text{eV}$  (assuming  $\Delta E_B/h = 10$  MHz). Such large valley splittings may exist in certain heterostructures, but are unlikely to be widespread across a device. In this work we simply take the conservative approach of assuming no inter-valley relaxation; any nonzero valley relaxation would improve shuttling fidelities beyond what is described here.

### 2. Fidelity metrics

To quantify the fidelity of our shuttling simulations, we compute the process fidelity, defined as [61]

$$F_{\text{process}}(U) = \frac{1}{d_1^2} |\text{tr}\{V^\dagger U_{\text{trunc}}\}|^2, \quad (8)$$

where  $V$  is the target unitary in the spin subspace,  $U = U_{\mathbb{B} \rightarrow \mathbb{B}'} U_t$  is the full evolution operator, including the effects of non-adiabatic evolution,  $U_{\mathbb{B} \rightarrow \mathbb{B}'}$  is the transformation matrix from the initial to the instantaneous eigenbasis,  $U_t$  is the evolution operator in the initial eigenbasis of our model, and the subscript ‘trunc’ denotes trun-



cation to the two-dimensional ( $d_1 = 2$ ) spin subspace of the instantaneous valley ground state. Equation (8) compares the evolution of a real shuttling process to an ideal, adiabatic process, while accounting for leakage errors, which can be independently quantified as [61]

$$L = 1 - \text{tr} \left\{ U_{\text{trunc}}^\dagger U_{\text{trunc}} \right\} / d_1. \quad (9)$$

When applying Eq. (8), we note that  $g$ -factor fluctuations cause random phases to accumulate during shuttling, even when the system remains in the ground state. Since such fluctuations are static, they can be compensated in experiments. It is therefore reasonable to remove these phase shifts from our fidelity estimates. We do this here by setting  $V = \mathbb{1}$  and optimizing the phase of  $U_{\text{trunc}}$  to maximize the fidelity. On the other hand, phase differences between the ground and excited valley states represent true dephasing errors, and cannot be removed. However, as no valley relaxation is assumed, these errors only directly affect  $U_{\text{trunc}}$  through a (weak) second-order Landau-Zener process, involving valley excitation followed by de-excitation. Thus, although leakage formally sets a lower bound on the infidelity (defined as  $I = 1 - F$ ), to a good approximation, we find that  $I \approx L$ . Our four-level shuttling fidelity calculations could therefore be replaced by a two-level problem involving just the valley levels. For better accuracy, we still perform four-level calculations using Eq. (8); however, we expect leakage to be the dominant source of infidelity.

### 3. Computational framework

The following computational procedure is used in our simulations. First, we calculate the time evolution of Eq. (7) using the software package `qopt`, described in [62]. The total propagator of the time evolution is calculated by splitting up the matrix exponential into a product of piecewise-constant Hamiltonians with appropriately small time steps. These time steps are chosen in the range of 2-4ps, depending on the quantum well and the shuttling velocity, to achieve sufficient convergence of the final results. After obtaining the propagator, the fidelity is computed from Eq. (8) and post-optimized as described above, using the python routine `jax.scipy.optimize.minimize` to perform phase calibration.

## C. Tuning strategies

In Figs. 3(b)-3(e), we illustrate the four tuning strategies used in this work to suppress valley excitations when shuttling near points of low valley splitting: (1) elongating the quantum dot along the shuttling trajectory while squeezing it in the transverse direction (this keeps the total dot area fixed, to allow a fair comparison with other

strategies, and ensures that the elongated electron wavefunction sees the same amount of Ge, on average), (2) shifting the lateral position of the dot within the shuttling channel, (3) modifying the shuttling velocity, and (4) varying the vertical electric field of the dot. The effects of these strategies can be understood intuitively as follows. Methods (2) and (4) simply avoid the points of low  $E_v$ . Method (3) directly suppresses the Landau-Zener tunneling process. Method (1) causes the dot to see less change in its average alloy environment for a given velocity, resulting in a lower *effective* velocity. Appendix I elaborates further on the physics of the elongation strategy. The final results obviously depend quantitatively on the imposed parameter constraints. Here we have chosen experimentally reasonable constraints; an exploration of different parameter ranges is given in Appendix C.

## V. RESULTS

### A. Evolution without applying tuning strategies

As a baseline, we first characterize spin shuttling across a spatially varying valley-splitting landscape, at a velocity of 5 m/s, without applying any fine-tuning strategies. Figure 4(a) shows the medians (markers) and 25-75 percentile ranges (bars) of the infidelity, computed according to Eq. (8), for 300 shuttling simulations, each with a different, random valley-splitting landscape. The results are reported as a function of position along the shuttling trajectory. (Here, we only show results for the initial 1  $\mu\text{m}$  portion of the trajectory.) We include results for the 10 nm, 3 nm, and 5% Ge quantum wells illustrated in Fig. 3(a). Despite experiencing different average valley splittings, these three heterostructures exhibit similar behaviors, characterized by a rapid increase of the infidelity over short distances, to levels that are incompatible with quantum computing on a sparse-grid architecture [22]. The main contribution to the infidelities observed in these simulations is the Landau-Zener excitation of the upper valley state, caused by momentary dips in  $E_v$ , as illustrated in Figs. 2(e) and 2(f). The simplest approach for suppressing such excitations is to uniformly reduce the shuttling velocity, which unfortunately leads to a competition between the shuttling and decoherence timescales. Other suppression strategies are therefore required, which we now include in our simulations.

### B. Electric-field modulation

Local modulation of the vertical electric field  $E_z$  causes the electron wavefunction to shift vertically, as illustrated in Fig. 3(e), exposing it to a slightly different Ge distribution, and modifying its valley splitting [41]. It may therefore be beneficial to modify  $E_z$  when a low valley-splitting region is encountered. While any  $E_z$  value can be used in

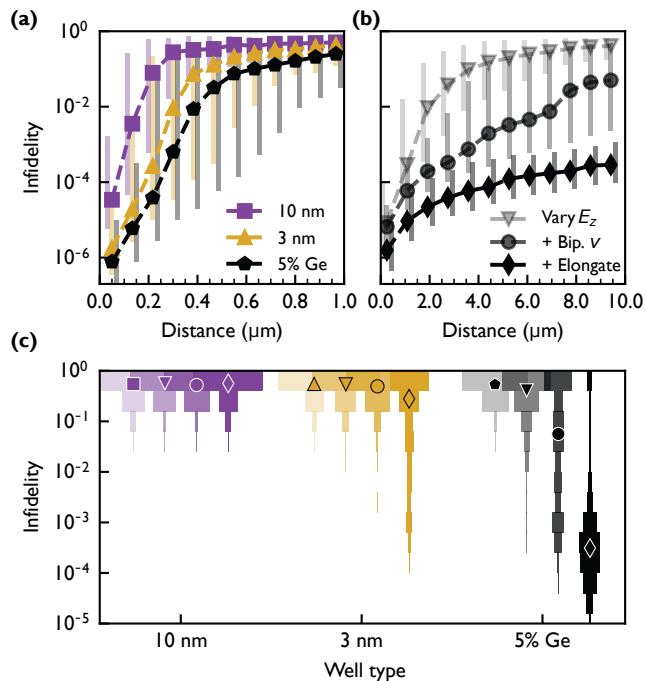


FIG. 4. A comparison of shuttling infidelities: (a) without, vs (b) with several of the tuning strategies depicted in Figs. 3(b)-3(e), for an average shuttling velocity of 5 m/s. (a) Infidelity as a function of shuttling distance, for the three quantum wells shown in Fig. 3(a). (b) Infidelity computed using the following tuning strategies, for the 5% Ge quantum well: (i)  $E_z$  modulation only (gray triangles); (ii)  $E_z$  modulation plus bipartite velocity modulation (dark-gray circles); or (iii)  $E_z$  modulation, bipartite velocity modulation, and elongated dots (black diamonds). For (a) and (b), the markers represent the median values obtained from 300 different disorder realizations, while the vertical bars show the 25-75 percentiles. (Note the different horizontal scales.) (c) Histograms of results like those shown in (a) and (b), for the full shuttling distance of  $10 \mu\text{m}$ , in all three quantum wells (color coded). Within each color grouping, the tuning methods are coded with the same marker styles as in (a) and (b). Only the 5% Ge well, with either two or three tuning strategies (last two histogram columns), provides significant improvements of the shuttling fidelity.

the simulations, we adopt some procedural constraints, to make our theoretical methods more compatible with experiments, and to reduce computing times. First, we restrict the  $E_z$  range to lie between 0 and 10 mV/nm. ( $E_z < 0$  can also be considered, but does not change our results significantly.) We note that even larger changes in  $E_z$  may be possible when using a back gate. However, the range chosen here includes relatively high fields [33], and should therefore be sufficient for evaluating the feasibility of  $E_z$  modulations. Second, we do not allow the field to be adjusted continuously; rather, we assume piece-wise constant  $E_z$  values over  $1 \mu\text{m}$  segments. To optimize the  $E_z$  values used in each shuttling segment, for a given valley landscape, we apply a graph traversal algorithm,

as described in Appendix G. This path seeks to avoid regions of low valley splittings, while making as few changes to the tuning parameters as possible. In real devices with no a-priori knowledge of the valley splitting, such optimization would require either obtaining a high-resolution map of  $E_v(\mathbf{r})$  [46] or applying trial-and-error methods.

Simulation results for infidelity vs shuttling distance are presented in Fig. 4(b) (light-gray triangles) where we show results only for the 5% Ge quantum well. We assume a single, fixed velocity of 5 m/s, corresponding to a total shuttling time of  $2 \mu\text{s}$ , which is slightly shorter than commonly observed  $T_2^*$  times of a few microseconds [1, 3, 63, 64]. As indicated here, the  $E_z$  modulation procedure provides some improvement over the baseline results shown in Fig. 4(a) (note the different horizontal scales in these two panels); however, the shuttling infidelities remain quite poor over the full shuttling range of  $10 \mu\text{m}$ .

### C. Bipartite velocity modulation

To further improve the shuttling fidelity, we next consider velocity modulation as a tuning strategy for suppressing Landau-Zener excitations in regions of low valley splitting. In this case, we adopt the constraint that only two shuttling velocities are allowed (rather than a continuous range):  $v_{\text{fast}}$  and  $v_{\text{slow}} = v_{\text{fast}}/5$ . As described in Appendix C, the slower velocity is applied whenever  $E_v$  falls below a threshold value, defined as 10% of the mean value of  $E_v$ , or  $20 \mu\text{eV}$ , whichever is greater. These choices strike a balance between sufficiently reducing  $v_{\text{slow}}$  while retaining a reasonable total shuttling velocity. As a safety margin, we also apply  $v_{\text{slow}}$  within a  $\pm 10 \text{ nm}$  window around these valley-splitting minima, while setting the velocity to  $v_{\text{fast}}$  elsewhere. On average, since fewer than ten slow-downs occur per trace under these constraints, we still maintain an average velocity of approximately 5 m/s, which is nearly equal to  $v_{\text{fast}}$ . Results for such bipartite velocity modulations, combined with  $E_z$  modulations, are shown in Fig. 4(b) (dark-gray circles). By combining tuning strategies in this way, we obtain an approximate order of magnitude improvement in the fidelity for the 5% Ge quantum well, as compared to the case where only  $E_z$  is modulated. However, the error bars of the infidelity are seen to be quite large.

### D. Elongated dots

Finally, we consider the shuttling of an elongated quantum dot, in which the orbital confinement energy in the shuttling direction  $\hbar\omega_x$  is reduced from 2 to 1 meV (elongating the dot along  $\hat{x}$ ), while increasing the confinement energy in the transverse direction  $\hbar\omega_y$  from 2 to 4 meV (squeezing the dot along  $\hat{y}$ ). In the current work, we do not explore potential pitfalls of this elongation strategy, although they may occur in some settings [24]. Results



of such elongated-dot simulations, combined with  $E_z$  and velocity modulations, are shown in Fig. 4(b) (black diamonds). In this case, we obtain significant improvement over previous results, by over an order of magnitude for longer shuttling distances. Figure 4(c) summarizes the results of these simulations, including the base case, for all three types of quantum wells. It is interesting to note that, while simultaneously applying multiple strategies is found to improve the shuttling fidelity for the 5% Ge quantum well, much weaker improvements are found for the 10 nm and 3 nm quantum wells. In Appendix H, we show that this tepid response is a consequence of using the  $E_z$ -modulation strategy, because  $E_z$  does not provide effective tuning of  $E_v$  for the other two heterostructures.

### E. Channel shifting

Since the  $E_z$  modulation scheme is not found to be effective universally, we also explore the channel-shifting strategy, depicted in Fig. 3(c), where the position of the electron is shifted along  $\hat{y}$  to avoid regions of low valley splitting. We expect this method to be more effective than  $E_z$  modulation because  $E_v$  typically varies much more as a function of  $y$  than as a function of  $E_z$  within the parameter constraints we consider. Moreover, since lateral shifting is not sensitive to the vertical Ge confinement profile, we expect the effectiveness to depend only on the variability of the valley splitting  $\sigma_\Delta$ , rather than other features of the quantum well.

Similar to  $E_z$  modulation, we determine the optimal shuttling trajectory by applying a graph-traversal algorithm. In this case, we again consider a full 10  $\mu\text{m}$  shuttling channel formed of piecewise-constant 1  $\mu\text{m}$  segments. We also constrain the trajectory to lie within the channel width given by  $y = \pm 50$  nm. Figure 5(a) illustrates one such optimized shuttling trajectory for the case of a 5% Ge quantum well, where the valley-splitting landscape is shown as grayscale, with regions of  $E_v < 35$   $\mu\text{eV}$  highlighted in red. Here, the compromises caused by limiting the shifts to 1  $\mu\text{m}$  segments are easy to visualize, because not all red regions can be avoided. Figure 5(b) illustrates the complicated evolution of the inter-valley coupling  $\Delta$ , following along this same trajectory. While most of this evolution exhibits a sufficiently large  $|\Delta|$ , a small portion still approaches  $|\Delta| \approx 0$ , causing leakage. Averaging such results over 300 valley-splitting landscapes yields the infidelity results shown as green diamonds in Fig. 5(c). Here we observe immediate improvement over the  $E_z$  modulation; we even observe improvement over the best-case results in Fig. 4(b), obtained for the 5% Ge quantum well.

Taking the same approach as Fig. 4, we now include additional tuning methods in Fig. 5(c): the rust-colored circles show the combined results of channel-shifting and bipartite velocity modulation (using the same two velocities as Fig. 4), while the purple diamonds show the combined results of channel-shifting, velocity modulation, and dot

elongation. In each case, we observe some fidelity improvement. Results of these different tuning schemes are shown as histograms in Fig. 5(d) for all three types of quantum wells. Here the best results are obtained for the 3 nm and 5% Ge quantum wells, which have much higher average valley splittings to begin with. These two quantum wells show similar results when applying multiple tuning strategies, obtaining infidelities consistently below  $10^{-3}$ , except for a small minority of outlier cases. Importantly, the 5% Ge quantum well shows a low average infidelity when applying *only* the channel-shifting strategy, although a significant fraction of results still give poor fidelities. Finally we note that the 10 nm quantum well – with a small average valley splitting of 50  $\mu\text{eV}$  – experiences particularly small  $E_v$  minima too frequently to be compensated by any tuning method, for any reasonable velocity.

### F. Transport velocity

As previously noted, transport velocity plays an important role in determining the leakage during shuttling, since the probability of Landau-Zener excitations depends exponentially on velocity. This strong dependence is evident in Fig. 5(e), where we plot simulation results like those in Fig. 5(d) for the 5% Ge quantum well, but we now consider a range of velocities. As in Fig. 5(d), we adopt three tuning strategies, using the same color coding as before. Here, when bipartite velocity modulations are employed, we note that it is the *average* velocity that is reported on the horizontal axis. [The results shown in Fig. 5(d) correspond to the velocity of 5 m/s in Fig. 5(e).] As expected, we find that lower velocities cause less leakage, and the shuttling fidelity depends sensitively on the choice of velocity.

On the other hand, slower shuttling speeds also increase the risk of decoherence, so the velocity should be carefully chosen. Although we do not include decoherence directly in our shuttling model, we now provide analytical estimates, to illustrate the emergence of an optimal shuttling velocity. In Ref. [24], it was argued that the main sources of decoherence during shuttling are time-varying Overhauser magnetic fields and low-frequency charge noise, which both cause dephasing of the spin over the time scale  $T_2^*$ . The same reference obtains an approximate expression for the noise-induced shuttling infidelity, which we have adapted to the present context (note the slight difference from [24]), as discussed in Appendix B:

$$I \approx \frac{l_c L_s}{(v T_2^*)^2}, \quad (10)$$

where  $l_c$  denotes the correlation length of the quasistatic noise source,  $L_s=10$   $\mu\text{m}$  is the shuttling distance,  $v$  is the average velocity, and we note that motional narrowing has been taken into account [25].

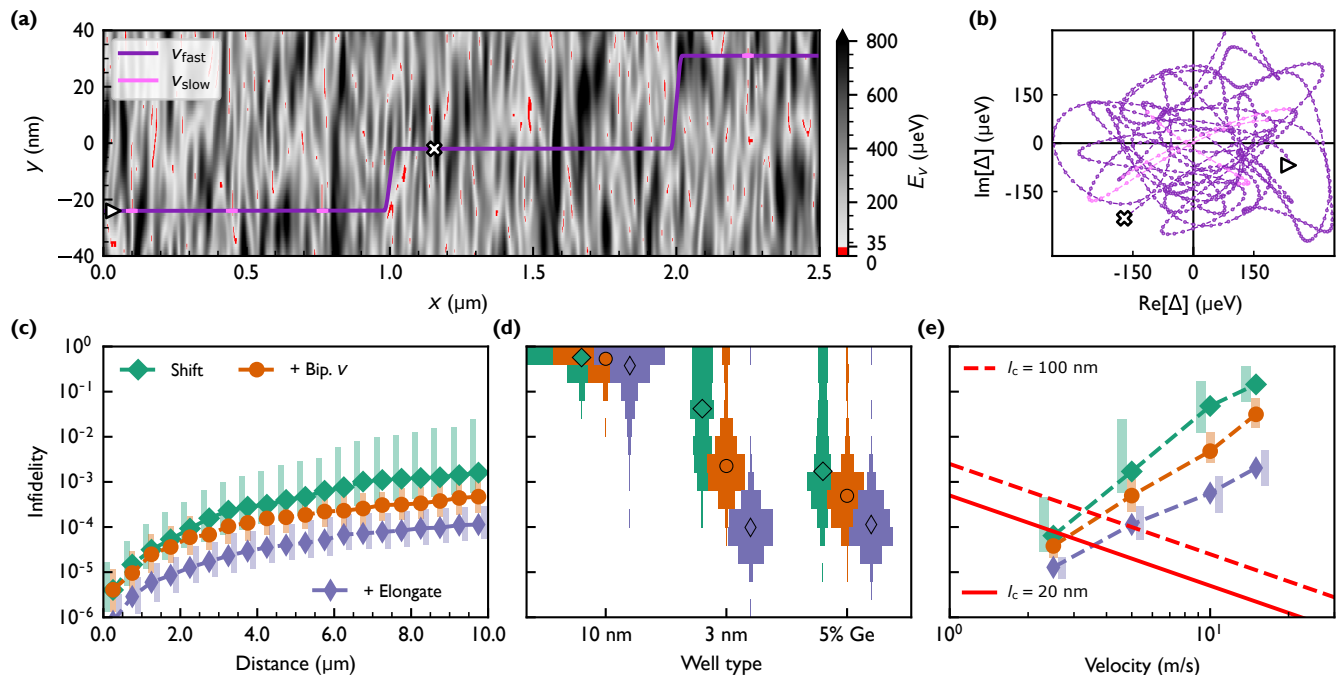


FIG. 5. Shuttling results involving lateral channel shifting. (a) Typical valley-splitting landscape for a 5% Ge quantum well, with regions of relatively low valley splitting highlighted in red (10% or less of the average value of  $E_v$ , or about  $35 \mu\text{eV}$ ). An optimized, segmented shuttling trajectory is shown in purple (see main text). In the few remaining regions of low valley splitting, the shuttling velocity may be reduced to  $v_{\text{slow}}$  (indicated in pink), to suppress Landau-Zener excitations. (b) Intervalley coupling  $\Delta$  along the same path shown in (a). (c) Shuttling infidelities computed using the following tuning strategies for the 5% Ge quantum well and average shuttling velocity 5 m/s: (i) lateral channel shifting only (green diamonds); (ii) channel shifting plus bipartite velocity modulation (rust-colored circles); or (iii) channel shifting, bipartite velocity modulation, and elongated dots (narrow violet diamonds). Here, the markers represent the median values obtained from 300 different disorder realizations, while the vertical bars show the 25-75 percentiles. (d) Histograms of results like those shown in (c), for the full shuttling distance of  $10 \mu\text{m}$ , in all three quantum wells. Here, the tuning methods are coded by both color and marker styles, as in (c). (e) Shuttling infidelities like those shown in (c), for the full shuttling distance of  $10 \mu\text{m}$ , as a function of average shuttling velocity. Downward-sloping lines show infidelity estimates for magnetic noise (solid red line) or charge noise (dashed red line), based on Eq. (10), with the indicated correlation lengths  $l_c$ .

In Fig. 5(e), we include two representative infidelity estimates from Eq. (10), obtained using  $l_c=20 \text{ nm}$  (solid red line), for the case where nuclear spin noise dominates, and  $l_c=100 \text{ nm}$  (dashed red line), for the case where charge noise dominates [24]. In both cases, we take a cautiously optimistic value of  $T_2^* \approx 20 \mu\text{s}$ , as consistent with Refs. [17, 63, 64]. This analysis confirms the presence of an optimal velocity value, which depends on the tuning strategies used and the dominant noise source, but generally corresponds to a few m/s. The analysis also shows that an appropriate choice of tuning strategies and velocities should yield, in principle, shuttling infidelities below  $10^{-3}$ .

### G. Sharp interfaces with steps

Up to this point, we have only considered quantum wells with valley splittings that are determined mainly by alloy disorder, since most current devices are expected to

fall into this regime [41]. For completeness, we also briefly consider the opposite regime, where alloy disorder plays a minor role. The most common quantum-well geometry for this purpose has a super-sharp interface, with an interface width of less than three atomic monolayers. For such geometries, the valley splitting should be enhanced, and the dominant form of disorder and  $E_v$  variability should arise from atomic steps at the quantum-well interface [41]. To study this situation, we perform simulations of shuttling with super-sharp interfaces and sparse step disorder, as described in Appendix A. Our results indicate that high-fidelity shuttling can be achieved in the presence of sparse step disorder, even without applying additional tuning methods. The fact that step disorder and alloy disorder can obtain such different results highlights the importance of including realistic disorder models that accurately account for random alloys.

## VI. IMPLEMENTING THE TUNING SCHEMES

We close by commenting on the added complexity that comes with the tuning methods proposed here, and their consequences for scalability. First, we note that dot size and shape in the elongation scheme are closely tied to the predetermined gate-electrode spacing. Some additional fine-tuning is possible; however, a truly scalable pulsing scheme favors applying the same ac signals to all the clavier gates across a quantum processor [19], suggesting that the dots (and the gate pitch) should all have a uniform size.

For the vertical or lateral channel-shifting schemes, we have proposed to divide the channel into smaller segments, which may then be manipulated in two ways, as we now explain. The most versatile approach involves manipulating each segment independently. For vertical shifting, this requires independent control of the clavier gates within each segment, while for lateral shifting it requires independent control of the screening gates in each segment. While such an approach is highly versatile, it also adds significant overhead to the wiring costs, effectively negating many of the global benefits of our shuttling scheme. The second approach involves applying tailored shift pulses to *all* the clavier gates or *all* the screening gates. This has the advantage of not requiring new control lines but has the disadvantage of affecting all the electrons within the conveyor. Thus, if multiple electrons are shuttled simultaneously, it would require a more-sophisticated path-traversal algorithm.

Similar considerations apply to bipartite velocity modulations, although we note that slow shuttling in a region with high valley splitting is harmless, so multi-electron shuttling is less fraught in this case. On the other hand, true global control could become a challenge, if a large number of slow-downs are needed.

Finally, we note that all proposed tuning strategies require the valley-splitting landscape to be carefully characterized. This characterization only needs to be performed once however. A recent experiment demonstrates that such mappings can be implemented effectively, within the same shuttling framework [46].

## VII. SUMMARY

In this work, we have shown that leakage from the ground valley to the excited valley state is a major source of decoherence for conveyor-mode spin shuttling in Si/SiGe quantum wells. This leakage is caused by Landau-Zener excitations across a narrow energy gap, as electrons traverse the wildly varying valley-splitting energy landscape caused by alloy disorder. In turn, leakage causes dephasing of the spin, due to the presence of different  $g$ -factors in the ground and excited valley states.

Using the most current understanding of random-alloy disorder, we perform simulations of the shuttling evolution within an effective 4D Hamiltonian spanning

the spin and valley degrees of freedom. For quantum wells falling into the “deterministically enhanced” valley-splitting regime (e.g., with interfaces narrower than three atomic monolayers), we find that Landau-Zener excitations do not pose a significant challenge for shuttling. It is hoped that such structures will become available for qubit implementations in the future.

Existing devices are not expected to fall into the deterministically enhanced regime, and our simulations indicate that coherent transport may be unfeasible in common 10 nm quantum wells in this “disorder-dominated” regime. In this case, we have also performed simulations of alternative quantum wells with much higher average valley splittings, including narrow 3 nm quantum wells and quantum wells with a significant concentration of Ge in the middle of the well. We have also explored a number of tuning strategies, including shifting the location of the electron inside the shuttling channel (either vertically or laterally), to avoid passing through a valley-splitting minimum, slowing down the shuttling velocity when it passes too close to a minimum, and elongating the quantum dot to change its effective velocity. In our simulations, we have optimized these tuning strategies, and we have also simultaneously applied multiple strategies, obtaining several orders of magnitude improvement in the shuttling fidelity. Since slower shuttling velocities suppress Landau-Zener excitations but lead to dephasing, we have also optimized the velocity, finding that velocities on the order of several m/s can provide shuttling infidelities below  $10^{-3}$ .

Finally, we note that the tuning strategies proposed here come with a nontrivial experimental overhead, which must be accounted for in scalable implementations. The valley-splitting landscape only needs to be mapped out once, however. In the future, we argue that fidelity-improving strategies like those considered here must be employed in any high-performance shuttling implementation in Si/SiGe quantum wells.

## ACKNOWLEDGMENTS

This research was sponsored in part by the Army Research Office (ARO) under Awards No. W911NF-17-1-0274, W911NF-22-1-0090, and W911NF-23-1-0110. The work was performed using the compute resources and assistance of the UW-Madison Center For High Throughput Computing (CHTC) in the Department of Computer Sciences. The CHTC is supported by UW-Madison, the Advanced Computing Initiative, the Wisconsin Alumni Research Foundation, the Wisconsin Institutes for Discovery, and the National Science Foundation, and is an active member of the OSG Consortium, which is supported by the National Science Foundation and the U.S. Department of Energy’s Office of Science. The work was also funded by the German Research Foundation (DFG) within the project 421769186 (SCHR 1404/5-1) and under Germany’s “Excellence Strategy - Cluster of

Excellence Matter and Light for Quantum Computing” (ML4Q) EXC 2004/1 – 390534769 and by the Federal Ministry of Education and Research under Contract No. FKZ: 13N14778. The views, conclusions, and recommendations contained in this document are those of the authors and are not necessarily endorsed nor should they be interpreted as representing the official policies, either expressed or implied, of the Army Research Office (ARO) or the U.S. Government. The U.S. Government is authorized to reproduce and distribute reprints for Government purposes notwithstanding any copyright notation herein.

### Appendix A: Super-sharp interfaces with atomic step disorder

In the main text, we considered the limit of disorder-dominated quantum wells, for which random-alloy disorder is the main source of variability in the valley splitting. In this Appendix, we consider the opposite, deterministically enhanced valley-splitting limit, which can be achieved, for example, in quantum wells with super-sharp interfaces. In this case, the dominant source of disorder is from single-atom steps at the quantum well interface. We now briefly show that such disorder from sparse steps has a very different effect on shuttling than random-alloy disorder, and that the resulting infidelities are greatly reduced in accordance with much larger minimal  $E_v$ .

When the QW interfaces are very sharp, monoatomic steps in the QW interfaces are the dominant source of  $E_v$  fluctuations. To study shuttling in this regime, we examine the case of a single atomic step, traversed at different shuttling velocities. We assume an orbital splitting of 2 meV and a vertical electric field of 5 mV/nm inside a well of width 10 nm, with perfectly sharp interfaces and a single atomic step in the interface. We use 2D effective mass theory to simulate the inter-valley coupling as the dot moves across the step (see Appendix D). The evolution of  $\Delta$  as the dot traverses the step is shown in Fig. 6(b), where at the step position, the dot has a minimum  $E_v$  of about 200  $\mu\text{eV}$ . We plot the resulting infidelity as function of shuttling distance in Fig. 6(a). We see spikes in the infidelity near the step position in Fig. 6(a). These correspond to the position with maximized  $|\partial_x \Delta|$ , the rate of change in  $\Delta$  as a function of distance, shown in Fig. 6(b). However, as the minimal  $E_v$  at the step position is much larger than typical minima present in the disordered regime, even velocities an order of magnitude higher than those considered in the main text converge to low infidelity values beyond the step. An ideal sharp interface with only occasional single monolayer steps can therefore enable high-fidelity transport even without applying tuning methods. It should be noted that multiple steps in close vicinity, i.e. on the order of the dot size, may decrease  $E_v^{\text{min}}$  again and induce larger infidelity, as considered in Ref. [24].

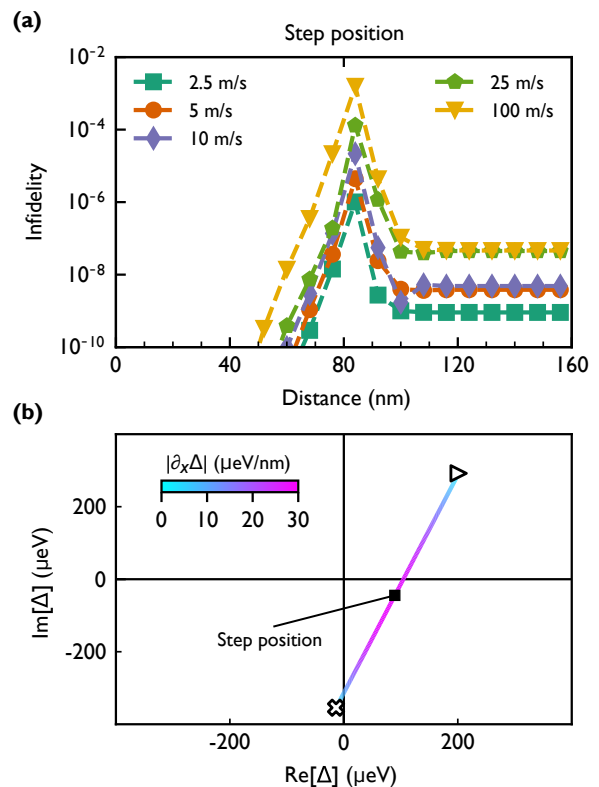


FIG. 6. Traversal of a single monoatomic step. (a) Infidelities as a function of shuttling distance, for a quantum well with a perfectly sharp interface containing a single atomic step centered in the middle of the shuttling path, for several different shuttling velocities (color coded). Working in the basis of instantaneous eigenstates, we observe an infidelity peak at the center of the Landau-Zener transition, as expected from theory [65, 66]. The infidelity then remains low after crossing the step, even for velocities up to 100 m/s. Compared to the disorder-dominated regime, this represents several orders of magnitude of improvement in the infidelity. (b) The inter-valley coupling  $\Delta$  plotted in the complex plane for the same shuttling path. Here, the lowest valley splitting occurs at the step location, with a value of 200  $\mu\text{eV}$ . The color code represents  $|\partial_x \Delta|$ .

### Appendix B: Prefactor of the noise-induced shuttling infidelity

Here, we briefly clarify the different prefactor appearing in Eq. (10), as compared to Ref. [24], which we have adapted to match the infidelity metric described in Sec. IV B 2. For a noise Hamiltonian given by

$$H_{\text{noise}} = \frac{\hbar}{2} \Phi(t) \sigma_z, \quad (\text{B1})$$

our metric can be rewritten as

$$F = \frac{1}{d^2} \left| \text{Tr} \left\{ \underbrace{V^\dagger}_1 U_{\text{noise}}(t) \right\} \right|^2 \quad (\text{B2})$$

$$= \frac{1}{d^2} \left| e^{i\Phi(t)/2} + e^{-i\Phi(t)/2} \right|^2, \quad (\text{B3})$$

where  $U_{\text{noise}}(t)$  is the time evolution operator for  $H_{\text{noise}}$ . Assuming a Gaussian ensemble average of qubit phases  $\Phi$  of zero mean and rms  $\delta\Phi$ , and with a dimension  $d = 2$ , this evaluates to

$$\langle F \rangle = \frac{1}{d^2} \left( 2 + 2e^{-\delta\Phi^2/2} \right) \quad (\text{B4})$$

$$\xrightarrow{d=2} \langle I \rangle = 1 - \langle F \rangle = \frac{1}{2} \left( 1 - e^{-\delta\Phi^2/2} \right) \approx \frac{\delta\Phi^2}{4}, \quad (\text{B5})$$

which implies an additional factor of 1/2 compared to Ref. [24].

### Appendix C: Parameter choices for two tuning methods

In this Appendix, we examine how parameter choices for two of the tuning strategies in the main text affect the shuttling infidelities. This discussion is not meant to provide a comprehensive analysis; rather, it is to illustrate some of the compromises that must be considered when making these choices.

We first examine how the segment length and channel width affect shuttling infidelities for the channel-shifting strategy. In Fig. 7(a), we modify both the length of each segment and the width of the shuttling channel (the ‘‘lateral range’’). We calculate the shuttling infidelities for the 3 nm QW at 10  $\mu\text{m}$  distance for each parameter choice, while simultaneously applying bipartite velocity modulation, with an average shuttling velocity of 5 m/s. As expected, both parameters have a significant effect on shuttling infidelities of at least several orders of magnitude. Increasing the lateral range makes it easier to avoid regions with low valley splittings, while smaller segment lengths allow for more frequent adjustments to the optimal path. For both parameters, the range of parameters considered in Fig. 7(a) does not result in asymptotic behavior of the infidelity; however, the range is imaginable for experimental realizations. On the other hand, the results suggest the existence of thresholds, beyond which the infidelities deteriorate significantly: for channel widths, this occurs below about 60 nm, and for segment lengths, it occurs above 1  $\mu\text{m}$ . The threshold for both parameters depends on the dot size, since valley splitting values are essentially uncorrelated when the dot is moved by the distance of a dot diameter. We therefore expect that smaller dots do not require a wide channel to achieve high shuttling fidelities; however they do require shorter segment lengths. At the threshold values for these tuning parameters, in addition to increasing

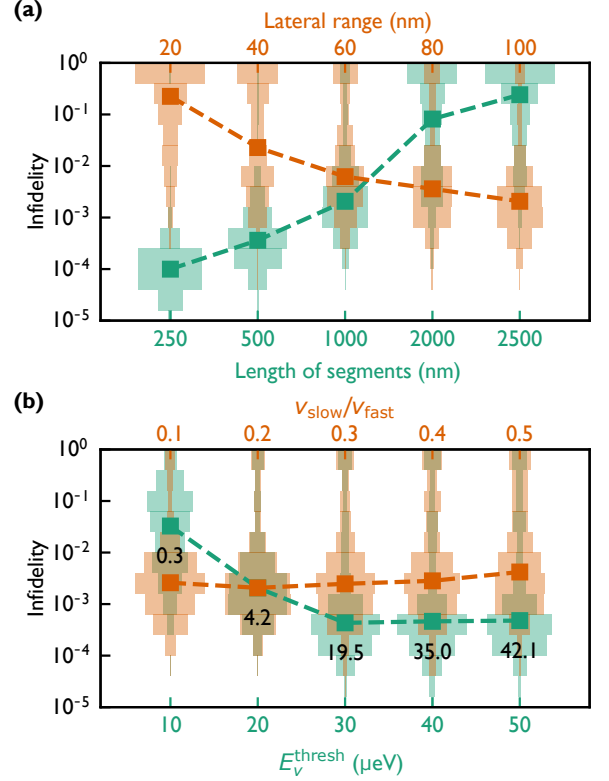


FIG. 7. Comparison of different simulation constraint parameters, for two tuning methods. (a) Exploration of shuttling infidelities as we vary parameters used in the channel-shifting simulations. Rust-colored histograms show results for several different lateral shift ranges. Green histograms show results for several different segment lengths. Larger lateral ranges and smaller segment lengths are seen to give higher fidelities. Here, results are obtained for a 10  $\mu\text{m}$  shuttling trajectory, for an average velocity of 5 m/s, in the 3 nm quantum well, and we simultaneously apply bipartite velocity modulation but no dot elongation. (b) Exploration of shuttling infidelities as we vary parameters related to bipartite velocity modulations. Rust-colored histograms show results for several values of the ratio  $v_{\text{slow}}/v_{\text{fast}}$ . Green histograms show results for several values of the threshold valley splitting  $E_v^{\text{thresh}}$ , below which the slower velocity is applied. While increasing the ratio  $v_{\text{slow}}/v_{\text{fast}}$  has a weak effect on the median infidelity values, it has a stronger effect on the number of very poor infidelity results. On the other hand, setting a low valley splitting threshold value causes the infidelity to increase significantly. Black numbers indicate the average number of valley splitting dips below  $E_v^{\text{min}}$  that occur over the full shuttle length. Other parameters are the same as in (a).

median infidelity, we note that the infidelity distribution also becomes problematic, with a much higher portion of infidelities occurring at higher values.

Second, we examine parameters related to bipartite velocity tuning. In Fig. 7(b), we analyze the choice of the ‘‘slow’’ velocity used near locations of low valley splitting,  $v_{\text{slow}}$ , and we study the choice of threshold valley

splitting,  $E_v^{\text{thresh}}$ , below which the velocity is reduced. Again, we consider simulations of the 3 nm QW evaluated at 10  $\mu\text{m}$ , with a fixed average velocity of 5 m/s, and we apply both bipartite velocity modulation and channel shifting techniques. We see that increasing the ratio  $v_{\text{slow}}/v_{\text{fast}}$  only slightly increases the median infidelity, but it significantly widens the tails of the distribution at large infidelities. Setting a higher threshold  $E_v^{\text{thresh}}$  for velocity switching causes the median infidelity to move to lower infidelities; however, this occurs at the cost of significantly more velocity switches per trace, as indicated by the black numbers accompanying the data points.

#### Appendix D: Effective-mass theory of valley splitting

In this section, we elaborate on the effective-mass envelope-function model for the valley states outlined in Refs. [40, 41] and referenced in Sec. III. We start with Eq. (2) in the main text, describing the inter-valley coupling  $\Delta$ . For a fully separable system, we can reduce Eq. (2) to a 1D integral over  $z$ . Moreover, following Refs. [40, 41], we transform the integral to a sum over atomic monolayers (MLs) to account for the discrete layers of the Si diamond cubic crystal structure, yielding Eq. (3) for  $\Delta_{1\text{D}}$  in the main text. When monoatomic steps are present at the interface, our system is no longer fully separable, and the reduction to 1D is no longer sufficient. In this case, we can easily generalize to 2D or 3D. For example, to simulate a system with a monoatomic step in the  $y$  direction, we can still separate the wavefunction as  $\psi_{\text{env}}(\mathbf{r}) = \psi_{\text{env}}(x, z)\psi_{\text{env}}(y)$ . By integrating over the  $y$  direction, we are then left with a 2D problem. Discretizing our system into cells of size  $(\Delta x, \Delta z) = (a_0, a_0/4)$  yields the 2D effective mass equation

$$\Delta_{2\text{D}} = \frac{a_0^2}{4} \sum_{j,l} e^{-2ik_0 z_l} U_{\text{qw}}(x_j, z_l) |\psi_{\text{env}}(x_j, z_l)|^2. \quad (\text{D1})$$

Here, the sum is over indices  $j$  and  $l$ , which label the  $x$  and  $z$  coordinates of each cell, respectively.

To a very good approximation, the quantum well potential  $U_{\text{qw}}$  is a linear function of the Ge concentration:

$$U_{\text{qw}}(\mathbf{r}) = \frac{X_{\mathbf{r}} - X_s}{X_w - X_s} \Delta E_c \quad (\text{D2})$$

where  $X_{\mathbf{r}}$  is the Si concentration at position  $\mathbf{r}$  in the heterostructure,  $X_w$  is the average Si concentration in the quantum well,  $X_s$  is the average Si concentration in the SiGe barrier/substrate region, and  $\Delta E_c$  is the conduction-band offset of the quantum well. For 1D systems, we can use  $X_{\mathbf{r}} = X_l$ , where  $l$  is the layer index. In this work, unless otherwise stated, we model our interfaces as sigmoid functions, where the average Si concen-

tration at layer  $l$  is defined by

$$\bar{X}_l = X_w + \frac{X_s - X_w}{1 + \exp[(z_l - z_t)/\tau]} + \frac{X_s - X_w}{1 + \exp[(z_b - z_l)/\tau]}, \quad (\text{D3})$$

where  $z_t$  and  $z_b$  label the positions of the top and bottom interfaces, and  $\lambda = 4\tau$  is the characteristic interface width. Unless otherwise specified, we use  $\lambda = 4\tau = 1$  nm.

In the case of monoatomic steps, the Si concentration  $X_{\mathbf{r}}$  adopts some lateral dependence. In this case, we can define the expected Si concentrations for a system with a step at lateral position  $x = 0$ :

$$\bar{X}_{j,l} = \bar{X}_l \Theta(x_j \leq 0) + \bar{X}_{l+1} \Theta(x_j > 0) \quad (\text{D4})$$

where  $\bar{X}_l$  is given by Eq. (D3) and  $\Theta(\cdot)$  is the Heaviside step function.

Both Eqs. (3) and (D1) depend on the envelope function  $\psi_{\text{env}}$ . To compute  $\psi_{\text{env}}$ , we discretize and solve a Schrodinger equation *without* valley physics. In the 1D case, we discretize and solve the effective 1D Hamiltonian

$$H_{1\text{D}} = -\frac{\hbar^2}{2m_l} \partial_z^2 + \bar{U}_{\text{qw}}(z) + U_\phi(z) \quad (\text{D5})$$

where  $m_l = 0.916m_e$  is the longitudinal effective mass of the electron,  $m_e$  is the bare electron mass,  $U_\phi(z) = eE_z z$  is the potential due to a vertical electric field  $E_z$ , and  $\bar{U}_{\text{qw}}$  is the quantum well potential without alloy-disorder-induced fluctuations. In the 2D case, we discretize and solve the effective 2D Hamiltonian

$$H_{2\text{D}} = -\frac{\hbar^2}{2m_l} \partial_z^2 - \frac{\hbar^2}{2m_t} \partial_x^2 + \bar{U}_{\text{qw}}(x, z) + U_\phi(z) + \frac{1}{2} m_t \omega_x^2 (x - x_0)^2 \quad (\text{D6})$$

where  $\omega_x$  is the orbital confinement energy in the  $x$ -direction, and  $x_0$  is the center location of the dot. In Appendix A, we considered shuttling across a mono-atomic step, where it was necessary to apply Eq. (D6). However, in the rest of this work, it is sufficient to use the 1D approximation of Eq. (D5).

To model the conduction-band offset, we follow Ref. [40]:

$$\Delta E_c = (X_w - X_s) \left[ \frac{X_w}{1 - X_s} \Delta E_{\Delta_2}^{\text{Si}}(X_s) - \frac{1 - X_w}{X_s} \Delta E_{\Delta_2}^{\text{Ge}}(X_s) \right], \quad (\text{D7})$$

where  $\Delta E_{\Delta_2}^{\text{Si(Ge)}}(X)$  are the  $\Delta_2$  conduction-band offsets for strained Si (Ge) grown on unstrained  $\text{Si}_X\text{Ge}_{1-X}$  substrate, and we approximate these functions as [67]

$$\begin{aligned} \Delta E_{\Delta_2}^{\text{Si}}(X) &\approx -0.502(1 - X) \text{ (eV)} \\ \Delta E_{\Delta_2}^{\text{Ge}}(X) &\approx 0.743 - 0.625(1 - X) \text{ (eV)}. \end{aligned} \quad (\text{D8})$$



Since the crystal lattice itself is composed of discrete atomic sites, the averaged concentration inside a finite-sized dot has an intrinsic uncertainty, given by  $X_l = \bar{X}_l + \delta_l$ , where  $\bar{X}_l$  is the mean Si concentration at layer  $l$ , and  $\delta_l$  is the fluctuation for a particular dot. The Si concentration  $X_l$  in layer  $l$  can be computed as a weighted average, where the contribution of each atom is weighted by the dot probability density at that atom:

$$X_l = \frac{1}{N_l} \sum_{a \in A_l} \mathbb{1}[a = \text{Si}] |\psi_{\text{env}}(a)|^2 = \bar{X}_l + \delta_l \quad (\text{D9})$$

where the sum is taken over  $A_l$ , the set of atoms in layer  $l$ ,  $\mathbb{1}[a = \text{Si}]$  is the indicator function that returns 1 if  $a$  is Si and 0 otherwise, and  $\psi_{\text{env}}(a)$  is the value of the envelope function at the position of atom  $a$ . The normalization constant  $N_l = \sum_{a \in A_l} |\psi_{\text{env}}(a)|^2$ . The inter-valley coupling of Eq. (3) can likewise be broken into fixed and random components  $\Delta_0$  and  $\delta\Delta$ :

$$\begin{aligned} \Delta_0 &= \frac{a_0 \Delta E_c}{4(X_w - X_s)} \sum_l e^{-2ik_0 z_l} (\bar{x}_l - x_s) |\psi_{\text{env}}(z_l)|^2, \\ \delta\Delta &= \frac{a_0 \Delta E_c}{4(X_w - X_s)} \sum_l e^{-2ik_0 z_l} \delta_l |\psi_{\text{env}}(z_l)|^2. \end{aligned} \quad (\text{D10})$$

In Eq. (D10),  $\Delta_0$  is the inter-valley coupling due to larger-scale features of the heterostructure, like the interface width or interface steps. On the other hand,  $\delta\Delta$  is a local fluctuation about  $\Delta_0$ , caused by alloy disorder. We can then compute the variance  $\sigma_\Delta^2 = \text{Var}[\delta\Delta]$ , as given in Eq. (4) in the main text.

### Appendix E: Generating valley-splitting landscapes

To obtain accurate statistics of shuttling fidelities, we need to generate many realistic examples of inter-valley couplings,  $\Delta$ , which vary spatially across the device. That is, we need many examples of  $\Delta(x, y)$ . To do so, we use the GSTools python library, which generates spatially random fields [68]. The real and imaginary components of  $\Delta$  are generated independently, with variances given by  $\sigma_\Delta^2/2$  and spatial covariances defined in Eq. (6).

The above approach works for spatially varying inter-valley couplings,  $\Delta(x, y)$ . However, to test the efficacy of modulating the electric field, we also need to generate many sample fields of the form  $\Delta(x, E_z)$ . Unlike the relationship between  $\Delta$  and  $x$ , the statistical relationship between  $\Delta$  and  $E_z$  is not given by a simple covariance equation that can be randomized. Instead, the effect of  $E_z$  depends on the shape of the quantum well interfaces, the quantum well width, and the Ge content in the quantum well. So, rather than randomly generating the field  $\Delta$ , we instead generate the local Si concentrations across the device, for each atomic layer of the quantum well. Since the dot is finite in extent, as it shuttles across the device, the effective Si concentrations experienced by the

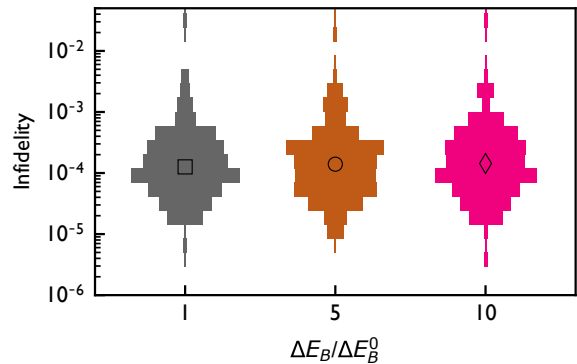


FIG. 8. Infidelity histograms for the channel-shifted 5% Ge quantum well, including all tuning methods applied, as in Fig. 5(d), as a function of the Zeeman splitting difference  $\Delta E_B$  between the ground and excited valley states. Here,  $\Delta E_B^0$  is the characteristic value of 10 MHz used in the main text.

dot at each layer in the heterostructure fluctuate slightly. Thus, the effective Si concentrations in the quantum well become position-dependent. We then indicate the Si concentration at layer  $l$  and lateral position  $x$  by  $X_l(x)$ . Using GSTools, we create many examples of  $X_l(x)$ . Then, for a given position and vertical field value, we use these local Si concentrations in our effective mass model, outlined above, to compute  $\Delta(x, E_z)$ . Below, we outline how we obtain these spatially fluctuating Si concentrations.

Previous work has shown that  $X_l$  can be approximately sampled from a binomial distribution,  $X_l \sim \frac{1}{N_{\text{eff}}} \text{Binom}(N_{\text{eff}}, \bar{X}_l)$ , where  $N_{\text{eff}} = 4\pi a_{\text{dot}}^2/a_0^2$  [41]. In turn, this is approximately equal to a normal distribution with mean  $\bar{X}_l$  and variance  $\sigma_X^2 = N_{\text{eff}} \bar{X}_l (1 - \bar{X}_l)$ . Therefore,  $X_l$  can be approximately sampled as

$$X_l \sim \frac{1}{N_{\text{eff}}} N(\bar{X}_l, N_{\text{eff}} \bar{X}_l (1 - \bar{X}_l)), \quad (\text{E1})$$

where  $N(\mu, \sigma^2)$  is the normal distribution with mean  $\mu$  and variance  $\sigma^2$ . The spatial covariance is then given by

$$\text{Cov}[X_l, X_l'] = \exp(-\delta_x^2/2a_x^2) \sigma_X^2, \quad (\text{E2})$$

where  $\delta_x$  indicates the distance between two points along the shuttling trajectory. Equations (E1) and (E2) describe the complete spatial statistics of  $X_l(x)$ , which we can input into GSTools, to generate fluctuating Si concentrations. Now, for each position  $x$ , we have a complete Si concentration profile  $X_l(x)$ , which we simulate using effective mass theory Eq. (3) to compute  $\Delta$ . Thus, we can build up sample fields of the form  $\Delta(x, E_z)$ .

### Appendix F: Dependence on $\Delta E_B$

We briefly comment on the dependence of the simulations on the difference in Zeeman splittings  $\Delta E_B$  between the ground and excited valley states. In Fig. 8, we

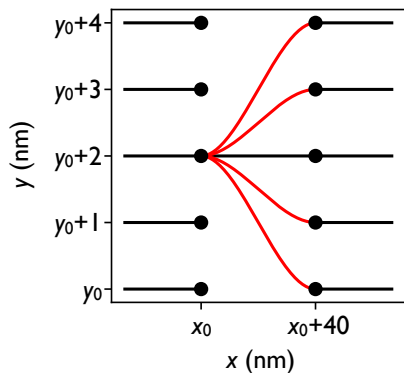


FIG. 9. Schematic illustration of the possible paths a dot can take across a device, implemented in our path traversal algorithm. Straight segments of fixed length are connected by transition zones of length 40 nm along the shuttling direction ( $\hat{x}$ ). The possible transitions from one such straight segment are illustrated, including the option to continue straight ( $\Delta p = \Delta y = 0$ ), shown in black, and the option to modify the parameter ( $|\Delta p| = |\Delta y| > 0$ ), shown in red.

illustrate the dependence of the shuttling infidelity distribution on  $\Delta E_B$  for the highest-fidelity simulations used in this work: shuttling in a 5% Ge quantum well with all tuning methods applied. We see that the distribution of infidelities changes only slightly when increasing the value of  $\Delta E_B$  by an order of magnitude. We can understand this result as follows. The metric used to evaluate the fidelity in this work considers, as a conservative assumption, only the population ending up in the ground state [61]. In the absence of fast relaxation dynamics, as discussed in the main text, we do not expect dots in the excited valley state to return to the ground state with significant probability. Since the energy scale of the  $\Delta E_B$  term has little effect on the Landau-Zener transition mechanism,  $\Delta E_B$  is not a determining factor for the infidelity results, as confirmed in Fig. 8.

### Appendix G: Path selection algorithm

To implement segmented channel-shifting strategies, we need to carefully choose our path across the valley splitting landscape, either by modifying the  $y$  coordinate of the dot or by modifying the vertical electric field  $E_z$ . In this work, we adopt a heuristic graph traversal algorithm to make this path selection. The valley splitting landscape is discretized into pixels of size  $1 \text{ nm} \times 1 \text{ nm}$  for  $y$  tuning, or  $0.1 \text{ mV/m} \times 1 \text{ nm}$  for  $E_z$ -tuning. To make use of common graph traversal algorithms, we define a graph representing the possible paths across this discretized landscape. The edges of the graph represent possible paths the dot could take across the device. These paths include straight segments of a fixed length with 40 nm transition zones between the segments. (We set all segment lengths to  $1 \mu\text{m}$  in this work, except briefly

in Appendix C.) [See Fig. 5(a) for an example trajectory, and Fig. 9 for an illustration of the method.] The parameter being optimized (either  $y$  or  $E_z$ ) remains constant along a straight segment (black lines in Fig. 9), but is modified smoothly and continuously in the transition zones (red lines in Fig. 9). Transitions between the optimized segments are heuristically defined as cubic polynomial functions whose derivatives go to zero at the endpoints of the transition.

An ideal path should have the following properties: (1) the minimum valley splitting along each segment should be large enough to avoid Landau-Zener transitions between the valley states, and (2) the transitions between segments should be as short as possible, to avoid increasing the effective shuttling velocity along long, steep transitions. To achieve paths that globally optimize these two properties, we assign weights  $w(e)$  to each edge  $e$  according to the following rules, which penalize both low minimum valley splittings ( $\min_e E_v$ ) along a given segment, and transitions with large changes  $\Delta p$  in the optimization parameter, where  $p = y$  or  $E_z$ :

$$w(e) = \begin{cases} 100 \cdot \frac{|\Delta p|}{\Delta p^{\max}} & \min_e E_v \geq T_v, \\ N + 100 \cdot \frac{|\Delta p|}{\Delta p^{\max}} + \frac{(T_v - \min_e E_v)^2}{1 \mu\text{eV}^2} & \min_e E_v < T_v, \end{cases} \quad (\text{G1})$$

where  $T_v$  is a threshold value for the valley splitting (measured in  $\mu\text{eV}$ ),  $\Delta p^{\max}$  is the maximum variation of  $p$  allowed between the segments, and  $N > 100$  is a large number chosen such that a transition edge with  $\min_e E_v \geq T_v$  has a smaller weight than a straight edge with  $\min_e E_v < T_v$ . We note that the exact values of the weights assumed in Eq. (G1) are relatively unimportant for our purposes, as long as both low- $E_v$  minima and transitions with large changes  $|\Delta p|$  are penalized, relative to paths with large minimum  $E_v$  and no transitions. In this work, we choose  $T_v = 50 \mu\text{eV}$  and  $N = 1000$ , with  $\Delta p^{\max} = 100 \text{ nm}$  for the channel-shifting protocol and  $\Delta p^{\max} = 10 \text{ mV/nm}$  for  $E$ -field modulation. After assigning weights to each edge in the graph, the graph traversal algorithm minimizes  $w$  to generate an optimized path across a given  $E_v$  landscape.

### Appendix H: Further characterization of the $E_z$ modulation strategy

In this Appendix, we further examine the performance of the electric-field ( $E_z$ ) modulation strategy. In Section VB, we highlighted that  $E_z$  modulation offers improvements in shuttling fidelity for 5% Ge quantum wells, but not for the other quantum wells analyzed in this work. We now explain these differences. First, for devices with sharp interfaces, it is well known that the valley splitting scales linearly with  $E_z$ , as stronger  $E_z$  increases the wavefunction penetration into the top barrier [69]. For more realistic quantum wells with diffuse interfaces, we expect the average valley splitting to also scale linearly with  $E_z$ , as increasing  $E_z$  forces the wavefunc-

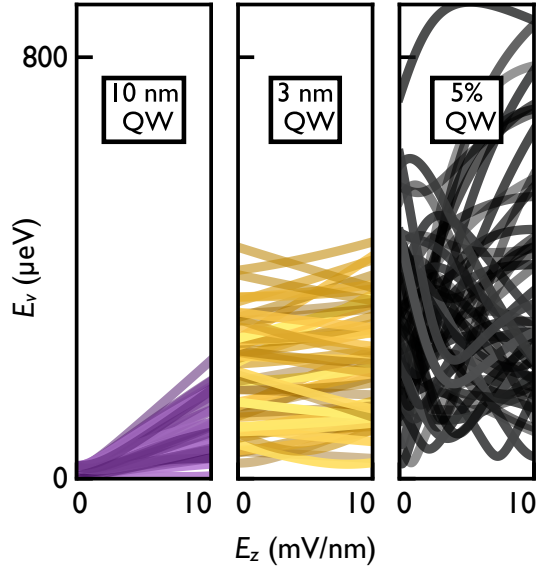


FIG. 10. Dependence of valley splitting on the vertical electric field, for the 10 nm quantum well (left), the 3 nm quantum well (middle), and the 5% Ge quantum well (right). Each plot shows the variation of  $E_v$  as a function of  $E_z$  for 100 instantiations of alloy disorder.

tion to overlap with more high-Ge layers [41]. However, for recently demonstrated heterostructures, like narrow quantum wells or quantum wells with a high Ge concentration,  $E_v$  has a nontrivial dependence on  $E_z$ , which we characterize below.

In Fig. 10, we show the variation of  $E_v$  as a function of  $E_z$  for 100 instantiations of each quantum well. For the 10 nm quantum well (left), we notice that  $E_v$  is largely monotonically increasing with  $E_z$ , since larger  $E_z$  pulls the dot strongly into the top barrier, increasing its overlap with high-Ge layers.

For the 3 nm quantum well (middle),  $E_v$  is no longer a monotonic function of  $E_z$ . Moreover, since the dot is tightly confined inside the narrow well, the dot position (and thus  $E_v$ ) is not very tunable as a function of  $E_z$ . In contrast, for the 5% Ge quantum well (right), the quantum well is much wider and has strong local fluctuations of the Ge concentration, so small shifts in the wavefunction position can significantly alter  $E_v$  as a function of  $E_z$ . In this case, if we want to use  $E_z$  as a tuning knob to avoid low- $E_v$  regions, this scheme can be very effective.

Figures 11(a)-11(c) show sample valley splitting landscapes as a function of position,  $x$ , and vertical field,  $E_z$ , for the case of (a) a 10 nm quantum well, (b) a 3 nm quantum well, and (c) a 5% Ge quantum well. In all plots, regions with  $E_v < 20 \mu\text{eV}$  are highlighted in red. As consistent with data in Fig. 10, we see in Fig. 11(a) that  $E_v$  tends to increase monotonically with  $E_z$ , for any location in a 10 nm quantum well. However, since this quantum well has a relatively low average  $E_v$ , despite the large vertical field, significant regions of low  $E_v$  cannot be avoided. Indeed, we see in Fig. 11(a) two  $x$  locations

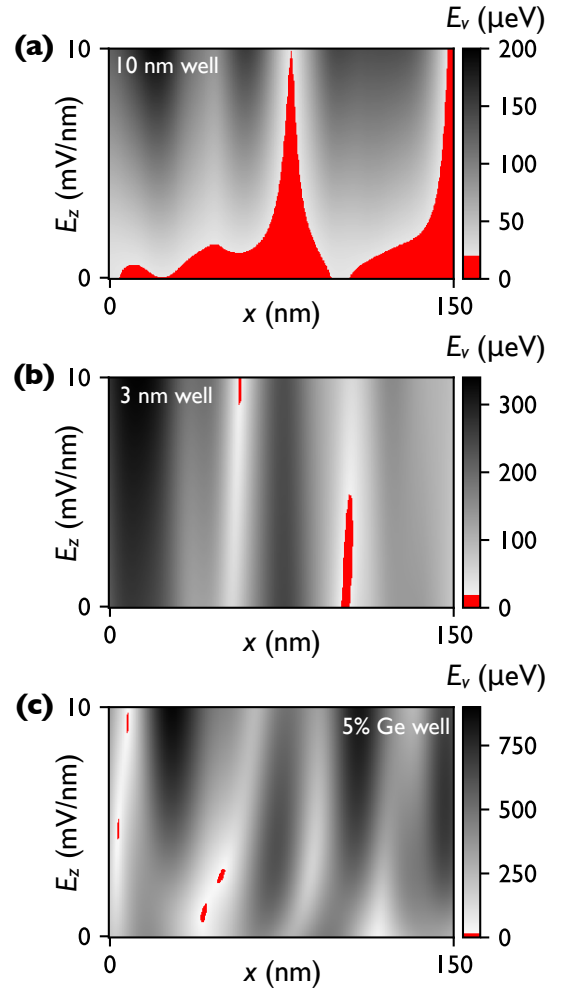


FIG. 11. Sample valley splitting landscapes as a function of position,  $x$ , and vertical field  $E_z$ , for (a) a 10 nm QW, (b) a 3 nm QW, and (c) a 5% Ge QW. In all panels, we highlight regions where  $E_v < 20 \mu\text{eV}$  in red.

where  $E_v < 20 \mu\text{eV}$  regardless of  $E_z$ . For the 3 nm well, we have a larger average  $E_v$ , and therefore fewer zones where  $E_v$  is dangerously small. However, since  $E_v$  is not highly tunable as a function of  $E_z$  in these quantum wells, regions of low  $E_v$  tend to persist over a wide range of  $E_z$ . When  $E_z$  is held constant over a distance of  $1 \mu\text{m}$ , these regions are difficult to avoid.

The situation is somewhat improved for the 5% Ge well in Fig. 11(c). First, the large amount of alloy disorder creates much larger average valley splittings. Additionally,  $E_v$  has a non-monotonic dependence on  $E_z$ , which makes it more likely that we can find an  $E_z$  value that avoids all low  $E_v$  for a given shuttling trajectory. We find, however, that taking advantage of such non-monotonicity requires imposing fairly short segments of constant  $E_z$ . If segments are too large, one is always likely to encounter low  $E_v$  values. Still, for the  $1 \mu\text{m}$  segments used in the simulations reported in the main text, we find  $E_z$  modulation does offer improved fidelities for

the 5% Ge quantum well.

### Appendix I: Further characterization of the dot-elongation strategy

In this Appendix, we provide further details on the performance of the dot-elongation tuning strategy. As a reminder, we have considered isotropic dots with orbital splittings  $\hbar\omega_x = \hbar\omega_y = 2$  meV, and “elongated” dots with orbital splittings  $\hbar\omega_x = 1$  meV and  $\hbar\omega_y = 4$  meV. While these choices yield dots with the same area, we find that they yield very different shuttling infidelities.

Elongating the dot in the shuttling direction has three main effects on the shuttling procedure. First, it increases the size of the dot along the shuttling direction, thereby reducing the effective length scale of the shuttling process. Since the characteristic length of valley splitting correlations depends entirely on the dot size, this means the moving dot will encounter proportionately fewer regions of low  $E_v$  on average. In Fig. 12(a), we plot the valley splitting for an isotropic (orange) vs an elongated (blue) dot, for the same landscape; here we can clearly see the longer correlation length scale in the blue data, and the larger number of regions with low  $E_v$  in the orange data. To create these plots, we generate an atomistic model of a heterostructure and raster the lateral confinement potential across this heterostructure, computing  $\Delta$  for each potential center  $x$ , using the method outlined in the main text. In Fig. 12(b), we histogram the number of local  $E_v$  minima observed along 300 straight shuttling trajectories, for both isotropic (yellow) and elongated (blue) dots. To avoid the massive computational overhead of populating 10  $\mu\text{m}$ -wide heterostructures atom-by-atom, we generate these  $E_v$  landscapes randomly, using the methods outlined in Appendix E. Results are shown for a trajectory length of 10  $\mu\text{m}$  in a 3 nm quantum well. Clearly, there are fewer local minima for elongated dots, leading to fewer opportunities for Landau-Zener excitations. Here, we also indicate the expected number of local minima in each case [vertical lines in Fig. 12(b)], as derived later in this Appendix.

The second effect of dot elongation is to increase the tunability of the valley splitting via the channel-shifting technique. Just as elongating the dot in the shuttling direction increases the characteristic length scale of valley splitting fluctuations along  $\hat{x}$ , narrowing the dot transverse to the shuttling trajectory reduces the characteristic fluctuation length scale along  $\hat{y}$ . Thus, for a fixed channel width, when we employ the channel-shifting strategy, the path-selection algorithm is effectively able to search over more variations in the  $E_v$  landscape, allowing it to identify better shuttling trajectories.

Finally, the third impact of elongating the dot is to reduce the effective shuttling velocity. This is important when passing through a narrow energy gap, because it reduces the probability of Landau-Zener excitations. To clarify this point, we examine the rate of change of the

inter-valley coupling of the moving dot,  $\partial_t\Delta$ . Using the chain rule, we have

$$\partial_t\Delta = v\partial_x\Delta = v(\partial_x\Delta_R + i\partial_x\Delta_I) \quad (I1)$$

where  $v$  is the shuttling velocity (assumed to be in the  $x$ -direction) and  $\Delta_{R/I}$  refer to the real and imaginary components of  $\Delta$ . The rate of change of  $\Delta$  is therefore directly related to the spatial derivative  $\partial_x\Delta$ . In Fig. 12(c), we plot histograms of  $|\partial_x\Delta|$  along 300 shuttling trajectories for the 3 nm quantum well, for both isotropic (yellow) and elongated (blue) dots, using the same set of landscapes as in (b). While both of these distributions exhibit some spread, the average gradient is clearly smaller for the elongated dots. Here, we also indicate the theoretically calculated mean gradients (vertical dashed lines) and probability density functions (solid lines) for  $|\partial_x\Delta|$ , as derived below.

*Calculation of the  $\partial_x\Delta$  distributions.* Since the inter-valley coupling  $\Delta$  fluctuates throughout the device, the derivatives on the right-hand-side of Eq. (I1) are random variables, and we may evaluate their statistics. To do so, we compute the variance of  $\partial_x\Delta$ :

$$\begin{aligned} \text{Var}[\partial_x\Delta] &= 2\text{Var}[\partial_x\Delta_R] \\ &= 2\text{Var}\left[\lim_{\delta_x \rightarrow 0} \frac{1}{\delta_x} (\Delta_R(x + \delta_x) - \Delta_R(x))\right] \\ &= 2 \lim_{\delta_x \rightarrow 0} \frac{1}{\delta_x^2} (\text{Var}[\Delta_R(x + \delta_x)] + \text{Var}[\Delta_R(x)] \\ &\quad - 2\text{Cov}[\Delta_R(x + \delta_x), \Delta_R(x)]) \\ &= 2 \lim_{\delta_x \rightarrow 0} \frac{1}{\delta_x^2} \left(\sigma_\Delta^2 - e^{-\delta_x^2/2a_x^2}\sigma_\Delta^2\right) \\ &= \frac{\sigma_\Delta^2}{a_x^2} \end{aligned} \quad (I2)$$

In the first line of Eq. (I2), we use the identity  $\text{Var}[A + iB] = \text{Var}[A] + \text{Var}[B]$  and the symmetry between  $\Delta_R$  and  $\Delta_I$ . In the second line, we use the definition of a derivative. In the third line, we interchange the order of the variance and the limit, and we use the identity  $\text{Var}[A - B] = \text{Var}[A] + \text{Var}[B] - 2\text{Cov}[A, B]$ . In the fourth line, we use  $\text{Var}[\Delta_R(x + \delta_x)] = \text{Var}[\Delta_R(x)] = \sigma_\Delta^2/2$ , and we use Eq. (6) to evaluate  $\text{Cov}[\Delta_R(x + \delta_x), \Delta_R(x)]$ . Finally, in the fifth line, we evaluate the limit. As consistent with the central-limit theorem, the quantity  $\partial_x\Delta$  is thus seen to be a circular complex Gaussian random variable, centered at the origin, with variance given by Eq. (I2).

Since  $\partial_x\Delta$  is complex, it is also interesting to evaluate the distribution of  $|\partial_x\Delta|$ . This quantity will have a Rayleigh distribution, whose probability density function is given by

$$p_{\text{Rayleigh}}(z) = \frac{z^2}{\sigma^2} \exp(-z^2/2\sigma^2), \quad (I3)$$

where we define the spread parameter as

$$\sigma = \frac{1}{2} \text{Var}[\partial_x\Delta] = \frac{\sigma_\Delta^2}{2a_x^2}. \quad (I4)$$

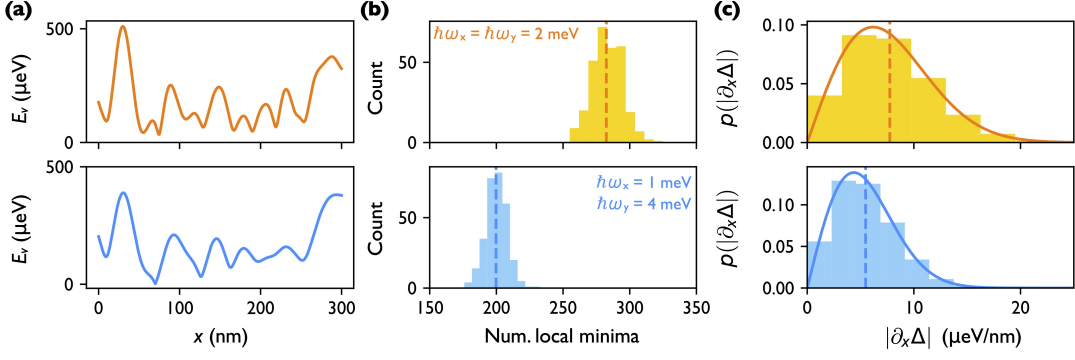


FIG. 12. Elongating the dot in the shuttling direction, and squeezing the dot in the transverse direction, reduces the magnitude of  $E_v$  fluctuations, significantly boosting shuttling fidelities. (a) Example  $E_v$  traces as a function of position for the 3 nm QW, for isotropic (top, orange) and elongated (bottom, blue) quantum dots. (b) Histograms of the number of local  $E_v$  minima along a 10  $\mu\text{m}$  shuttling path, for 300 iterations with the 3 nm QW, using isotropic (top, yellow) and elongated (bottom, blue) dots. Dashed lines indicate the expected number of local minima in each case ( $E[N] \approx 282$  for isotropic dots and  $\approx 200$  for elongated dots), computed with Eq. (I21). (c) Histograms of  $|\partial_x \Delta|$  across the same 300 shuttling trajectories. Solid lines indicate the theoretical probability density functions, computed with Eq. (I3). Dashed lines indicate the expected mean gradient,  $E[|\partial_x \Delta|]$ , computed with Eq. (I5), which are 7.7 for isotropic dots and 5.5 for elongated dots.

The probability density functions for  $|\partial_x \Delta|$  from Eq. (I3) are shown as solid lines in Fig. 12(c). The expected value of  $|\partial_x \Delta|$  is likewise given by

$$E[|\partial_x \Delta|] = \sqrt{\frac{\pi}{2}} \sigma. \quad (\text{I5})$$

Evaluating  $E[|\partial_x \Delta|]$  for the elongated and isotropic dots gives the results plotted as vertical dashed lines in Fig. 12(c).

*Estimating the number of valley-splitting minima.* We now compute the expected number of valley splitting minima along a straight shuttling trajectory. Typical results are shown with vertical dashed lines in Fig. 12(b). We follow the approach of Ref. [70], which we reproduce below for completeness. Note that we restrict the analysis to just one spatial dimension.

Using the Kac-Rice formula, the number of local minima is given by [71]

$$N = \frac{1}{2} \int_x dx \delta(\partial_x E_v^2) |\partial_x^2 E_v^2|, \quad (\text{I6})$$

where the factor of 1/2 accounts for the fact that half of the extrema points (where  $\partial_x E_v^2 = 0$ ) are minima, and  $\delta(\partial_x E_v^2)$  is a delta-function that activates when  $E_v^2$  is at an extremum. Using the identity

$$\delta(f(x)) = \sum_i \frac{\delta(x - x_i)}{|f'(x_i)|}, \text{ where } f(x_i) = 0, \quad (\text{I7})$$

we see that the remaining factor  $|\partial_x^2 E_v^2|$  allows the integral to count the number of extrema in  $E_v^2$ . Here, we use  $E_v^2$  instead of  $E_v$  to simplify the calculation, without changing the results. Mathematically, the quantity  $E_v^2$  is a  $\chi^2$  random field with two contributing Gaussian random fields,  $E_v^2 = 4\Delta_R^2 + 4\Delta_I^2$ . The derivatives of  $E_v^2$  are

given by

$$\begin{aligned} \partial_x E_v^2 &= 8\Delta_R \partial_x \Delta_R + 8\Delta_I \partial_x \Delta_I, \\ \partial_x^2 E_v^2 &= 8(\partial_x \Delta_R)^2 + 8\Delta_R \partial_x^2 \Delta_R + 8(\partial_x \Delta_I)^2 + 8\Delta_I \partial_x^2 \Delta_I. \end{aligned} \quad (\text{I8})$$

We compute the expectation value,  $E[N]$ , by averaging over all possible configurations of the inter-valley coupling:

$$\begin{aligned} E[N] &= \frac{1}{2} \int d\Phi P(\Phi) \int_x dx \\ &\quad \times \delta(8\Delta_R \partial_x \Delta_R + 8\Delta_I \partial_x \Delta_I) |\partial_x^2 E_v^2|, \end{aligned} \quad (\text{I9})$$

where we use  $\Phi$  as shorthand notation for the random field configurations of  $\Delta_R(x)$ ,  $\Delta_I(x)$ , and their derivatives. More explicitly, the integral element is given by

$$d\Phi = d\Delta_R d\Delta_I d(\partial_x \Delta_R) d(\partial_x \Delta_I) d(\partial_x^2 \Delta_R) d(\partial_x^2 \Delta_I), \quad (\text{I10})$$

and the total probability density function is given by

$$\begin{aligned} P(\Phi) &= P_{\Delta, \partial_x^2 \Delta}(\Delta_R, \partial_x^2 \Delta_R) P_{\Delta, \partial_x^2 \Delta}(\Delta_I, \partial_x^2 \Delta_I) \\ &\quad \times P_{\partial_x \Delta}(\partial_x \Delta_R) P_{\partial_x \Delta}(\partial_x \Delta_I). \end{aligned} \quad (\text{I11})$$

Note that we do not include higher order derivatives here, since they do not appear in the integrand. Also note that the random fields  $\Delta_R$  and  $\Delta_I$  are independent by definition, and any covariance of the form  $\langle \Delta_i(x) \partial_x \Delta_j(x) \rangle$  or  $\langle \partial_x^2 \Delta_i(x) \partial_x \Delta_j(x) \rangle$  must vanish due to the  $x \rightarrow -x$  symmetry of the integral, where we use angle brackets  $\langle \cdot \rangle$  to denote the expectation value of a quantity over its field configurations. Thus, we are left with two probability density functions to compute: one for the first derivatives of the field,  $P_{\partial_x \Delta}(\partial_x \Delta_j)$ , as well as the joint probability

density function for the fields and their second derivatives,  $P_{\Delta, \partial_x^2 \Delta}(\Delta_j, \partial_x^2 \Delta_j)$ . We showed above that  $\partial_x \Delta_R$  and  $\partial_x \Delta_I$  are Gaussian random variables with zero mean and variance  $\sigma_\Delta^2/2a_x^2$ . We therefore have

$$P_{\partial_x \Delta}(\partial_x \Delta_j) = \frac{a_x}{\sqrt{\pi} \sigma_\Delta} \exp\left(-(\partial_x \Delta_j)^2 a_x^2 / \sigma_\Delta^2\right). \quad (\text{I12})$$

Finally, we compute  $P_{\Delta, \partial_x^2 \Delta}(\Delta_j, \partial_x^2 \Delta_j)$ . To do this, we need covariances of the form  $\langle \Delta_j(x) \partial_x^2 \Delta_j(x) \rangle$ . By expressing the random fields in the reciprocal basis,

$$\Delta_j = \int \frac{dk}{2\pi} e^{ikx} \tilde{\Delta}_j(k), \quad (\text{I13})$$

we can evaluate

$$\langle \Delta_j(x) \partial_x^2 \Delta_j(x) \rangle = -\frac{1}{2\pi} \int dk k^2 P(k), \quad (\text{I14})$$

where the power spectrum  $P(k)$  is the Fourier transform of the covariance function  $\langle \Delta_j(x) \Delta_j(x') \rangle$ , which is provided in Eq. (6). Hence, we find

$$P(k) = a_x \sigma_\Delta^2 \sqrt{\pi/2} \exp(-a_x^2 k^2 / 2). \quad (\text{I15})$$

We then evaluate Eq. (I14), obtaining

$$\langle \Delta_j(x) \partial_x^2 \Delta_j(x) \rangle = -\frac{\sigma_\Delta^2}{2a_x^2}. \quad (\text{I16})$$

Using the same technique, we can evaluate the variance as

$$\langle (\partial_x^2 \Delta_j(x))^2 \rangle = \frac{1}{2\pi} \int dk k^4 P(k) = \frac{3\sigma_\Delta^2}{2a_x^4}. \quad (\text{I17})$$

---


$$E[N] = \frac{1}{2} \int_x dx \int d\Delta_R d\Delta_I d(\partial_x \Delta_R) d(\partial_x^2 \Delta_R) d(\partial_x^2 \Delta_I) \\ \times P_{\Delta, \partial_x^2 \Delta}(\Delta_R, \partial_x^2 \Delta_R) P_{\Delta, \partial_x^2 \Delta}(\Delta_I, \partial_x^2 \Delta_I) P_{\partial_x \Delta}(\partial_x \Delta_R) P_{\partial_x \Delta} \left( \frac{-\Delta_R \partial_x \Delta_R}{\Delta_I} \right) |\partial_x^2 E_v^2| (|\delta \Delta_I|)^{-1}. \quad (\text{I20})$$

Here, the probability density functions are given in Eq. (I12) and Eq. (I18), and the term  $|\partial_x^2 E_v^2|$  is given in Eq. (I8). The final term  $(|\delta \Delta_I|)^{-1}$  comes from the evaluation of the  $\delta$ -function, where we have used Eq. (I7).

Since the fields  $\Delta_j$  and their derivatives are Gaussian random variables with zero mean, we can define the joint probability density function as

$$P_{\Delta, \partial_x^2 \Delta}(\Delta_j, \partial_x^2 \Delta_j) \\ = \frac{1}{\sqrt{(2\pi)^2 |\Sigma|}} \exp\left(-\frac{1}{2} \mathbf{v}^T \Sigma^{-1} \mathbf{v}\right) \\ = \frac{a_x^2}{\sqrt{2\pi} \sigma_\Delta^2} \exp\left(-\frac{3\Delta_j^2 + 2a_x^2 \Delta_j \partial_x^2 \Delta_j + a_x^4 (\partial_x^2 \Delta_j)^2}{2\sigma_\Delta^2}\right), \quad (\text{I18})$$

where  $\mathbf{v}^T = (\Delta_j, \partial_x^2 \Delta_j)$  and the covariance matrix is given by

$$\Sigma = \frac{\sigma_\Delta^2}{2} \begin{pmatrix} 1 & -a_x^{-2} \\ -a_x^{-2} & 3a_x^{-4} \end{pmatrix}. \quad (\text{I19})$$

Here, we used Eq. (I16) to populate the off-diagonal elements of  $\Sigma$ , and Eq. (I17) to populate the remaining diagonal element.

We are then in a position to evaluate Eq. (I9). First, we eliminate the  $\delta$ -function and the integral over  $\partial_x(\Delta_I)$  by setting  $\partial_x \Delta_I = -\Delta_R \partial_x \Delta_R / \Delta_I$ , which yields

---

Finally, we evaluate Eq. (I20) numerically, obtaining

$$E[N] \approx 0.4 \times \frac{x_{\text{tot}}}{a_x}, \quad (\text{I21})$$

where  $x_{\text{tot}}$  is the total shuttling distance. The dashed lines indicating  $E[N]$  in Fig. 12(b) were computed using Eq. (I21). Since  $E[N]$  scales as  $1/a_x$ , we see that reducing the orbital energy from 2 to 1 meV, should cause  $E[N]$  to drop by a factor of  $1/\sqrt{2}$ .

---

[1] A. Noiri, K. Takeda, T. Nakajima, T. Kobayashi, A. Sammak, G. Scappucci, and S. Tarucha, Fast universal quan-

tum gate above the fault-tolerance threshold in silicon,



- Nature **601**, 338 (2022).
- [2] X. Xue, M. Russ, N. Samkharadze, B. Undseth, A. Sammak, G. Scappucci, and L. M. K. Vandersypen, Quantum logic with spin qubits crossing the surface code threshold, Nature **601**, 343 (2022).
- [3] A. R. Mills, C. R. Guinn, M. J. Gullans, A. J. Sigillito, M. M. Feldman, E. Nielsen, and J. R. Petta, Two-qubit silicon quantum processor with operation fidelity exceeding 99%, Science Advances **8**, eabn5130 (2022).
- [4] L. Trifunovic, O. Dial, M. Trif, J. R. Wootton, R. Abebe, A. Yacoby, and D. Loss, Long-distance spin-spin coupling via floating gates, Phys. Rev. X **2**, 011006 (2012).
- [5] F. R. Braakman, P. Barthelémy, C. Reichl, W. Wegscheider, and L. M. K. Vandersypen, Long-distance coherent coupling in a quantum dot array, Nature Nanotechnology **8**, 432 (2013).
- [6] M. Serina, C. Kloeffer, and D. Loss, Long-range interaction between charge and spin qubits in quantum dots, Phys. Rev. B **95**, 245422 (2017).
- [7] G. Tosi, F. A. Mohiyaddin, V. Schmitt, S. Tenberg, R. Rahman, G. Klimeck, and A. Morello, Silicon quantum processor with robust long-distance qubit couplings, Nature Communications **8**, 450 (2017).
- [8] N. Samkharadze, G. Zheng, N. Kalhor, D. Brousse, A. Sammak, U. Mendes, A. Blais, G. Scappucci, and L. Vandersypen, Strong spin-photon coupling in silicon, Science **359**, 1123 (2018).
- [9] A. Warren, E. Barnes, and S. E. Economou, Long-distance entangling gates between quantum dot spins mediated by a superconducting resonator, Phys. Rev. B **100**, 161303 (2019).
- [10] H. Qiao, Y. P. Kandel, S. Fallahi, G. C. Gardner, M. J. Manfra, X. Hu, and J. M. Nichol, Long-distance superexchange between semiconductor quantum-dot electron spins, Phys. Rev. Lett. **126**, 017701 (2021).
- [11] N. Holman, D. Rosenberg, D. Yost, J. L. Yoder, R. Das, W. D. Oliver, R. McDermott, and M. A. Eriksson, 3d integration and measurement of a semiconductor double quantum dot with a high-impedance TiN resonator, npj Quantum Information **7**, 137 (2021).
- [12] Z. Wang, M. Feng, S. Serrano, W. Gilbert, R. C. C. Leon, T. Tanttu, P. Mai, D. Liang, J. Y. Huang, Y. Su, W. H. Lim, F. E. Hudson, C. C. Escott, A. Morello, C. H. Yang, A. S. Dzurak, A. Saraiva, and A. Laucht, Jellybean quantum dots in silicon for qubit coupling and on-chip quantum chemistry, Advanced Materials **35**, 2208557 (2023).
- [13] A. J. Landig, J. V. Koski, P. Scarlino, U. Mendes, A. Blais, C. Reichl, W. Wegscheider, A. Wallraff, K. Ensslin, and T. Ihn, Coherent spin-photon coupling using a resonant exchange qubit, Nature **560**, 179 (2018).
- [14] A. Sigillito, M. Gullans, L. Edge, M. Borselli, and J. Petta, Coherent transfer of quantum information in a silicon double quantum dot using resonant swap gates, npj Quantum Information **5**, 110 (2019).
- [15] T. Fujita, T. A. Baart, C. Reichl, W. Wegscheider, and L. M. K. Vandersypen, Coherent shuttle of electron-spin states, npj Quantum Information **3**, 22 (2017).
- [16] A. Mills, D. Zajac, M. Gullans, F. Schupp, T. Hazard, and J. Petta, Shuttling a single charge across a one-dimensional array of silicon quantum dots, Nature Communications **10**, 1063 (2019).
- [17] J. Yoneda, W. Huang, M. Feng, C. H. Yang, K. W. Chan, T. Tanttu, W. Gilbert, R. Leon, F. Hudson, K. Itoh, *et al.*, Coherent spin qubit transport in silicon, Nature Communications **12**, 4114 (2021).
- [18] B. Jadot, P.-A. Mortemousque, E. Chanrion, V. Thiney, A. Ludwig, A. D. Wieck, M. Urdampilleta, C. Bäuerle, and T. Meunier, Distant spin entanglement via fast and coherent electron shuttling, Nature Nanotechnology **16**, 570 (2021).
- [19] I. Seidler, T. Struck, R. Xue, N. Focke, S. Trellenkamp, H. Bluhm, and L. R. Schreiber, Conveyor-mode single-electron shuttling in Si/SiGe for a scalable quantum computing architecture, npj Quantum Information **8**, 100 (2022).
- [20] A. Noiri, K. Takeda, T. Nakajima, T. Kobayashi, A. Sammak, G. Scappucci, and S. Tarucha, A shuttling-based two-qubit logic gate for linking distant silicon quantum processors, Nature Communications **13**, 5740 (2022).
- [21] J. M. Boter, J. P. Dehollain, J. P. G. Van Dijk, Y. Xu, T. Hensgens, R. Versluis, H. W. L. Naus, J. S. Clarke, M. Veldhorst, F. Sebastiano, *et al.*, Spiderweb array: a sparse spin-qubit array, Physical Review Applied **18**, 024053 (2022).
- [22] M. Künne, A. Willmes, M. Oberländer, C. Gorjaew, J. D. Teske, H. Bhardwaj, M. Beer, E. Kammerloher, R. Otten, I. Seidler, *et al.*, The spinbus architecture: Scaling spin qubits with electron shuttling, arXiv preprint arXiv:2306.16348 (2023).
- [23] A. M. J. Zwerver, S. V. Amitonov, S. L. de Snoo, M. T. Mađzik, M. Rimbach-Russ, A. Sammak, G. Scappucci, and L. M. K. Vandersypen, Shuttling an electron spin through a silicon quantum dot array, PRX Quantum **4**, 030303 (2023).
- [24] V. Langrock, J. A. Krzywda, N. Focke, I. Seidler, L. R. Schreiber, and Ł. Cywiński, Blueprint of a scalable spin qubit shuttle device for coherent mid-range qubit transfer in disordered Si/SiGe/SiO<sub>2</sub>, PRX Quantum **4**, 020305 (2023).
- [25] T. Struck, M. Volmer, L. Visser, T. Offermann, R. Xue, J.-S. Tu, S. Trellenkamp, Ł. Cywiński, H. Bluhm, and L. R. Schreiber, Spin-EPR-pair separation by conveyor-mode single electron shuttling in Si/SiGe, Nature Communications **15**, 1325 (2024).
- [26] R. Xue, M. Beer, I. Seidler, S. Humpohl, J.-S. Tu, S. Trellenkamp, T. Struck, H. Bluhm, and L. R. Schreiber, Si/SiGe QuBus for single electron information-processing devices with memory and micron-scale connectivity function, Nature Communications **15**, 2296 (2024).
- [27] F. A. Zwanenburg, A. S. Dzurak, A. Morello, M. Y. Simmons, L. C. L. Hollenberg, G. Klimeck, S. Rogge, S. N. Coppersmith, and M. A. Eriksson, Silicon quantum electronics, Rev. Mod. Phys. **85**, 961 (2013).
- [28] G. Burkard, T. D. Ladd, A. Pan, J. M. Nichol, and J. R. Petta, Semiconductor spin qubits, Reviews of Modern Physics **95**, 025003 (2023).
- [29] M. G. Borselli, R. S. Ross, A. A. Kiselev, E. T. Croke, K. S. Holabird, P. W. Deelman, L. D. Warren, I. Alvarado-Rodriguez, I. Milosavljevic, F. C. Ku, W. S. Wong, A. E. Schmitz, M. Sokolich, M. F. Gyure, and A. T. Hunter, Measurement of valley splitting in high-symmetry Si/SiGe quantum dots, Appl. Phys. Lett. **98**, 123118 (2011).
- [30] Z. Shi, C. B. Simmons, J. Prance, J. K. Gamble, M. Friesen, D. E. Savage, M. G. Lagally, S. N. Coppersmith, and M. A. Eriksson, Tunable singlet-triplet splitting in a few-electron Si/SiGe quantum dot, Appl. Phys. Lett. **99**, 233108 (2011).

- [31] D. Zajac, T. Hazard, X. Mi, K. Wang, and J. R. Petta, A reconfigurable gate architecture for Si/SiGe quantum dots, *Applied Physics Letters* **106**, 223507 (2015).
- [32] P. Scarlino, E. Kawakami, T. Jullien, D. R. Ward, D. E. Savage, M. G. Lagally, M. Friesen, S. N. Coppersmith, M. A. Eriksson, and L. M. K. Vandersypen, Dressed photon-orbital states in a quantum dot: Intervalley spin resonance, *Phys. Rev. B* **95**, 165429 (2017).
- [33] A. Hollmann, T. Struck, V. Langrock, A. Schmidbauer, F. Schauer, T. Leonhardt, K. Sawano, H. Riemann, N. V. Abrosimov, D. Bougeard, *et al.*, Large, tunable valley splitting and single-spin relaxation mechanisms in a Si/Si<sub>x</sub>Ge<sub>1-x</sub> quantum dot, *Phys. Rev. Applied* **13**, 034068 (2020).
- [34] X. Mi, C. G. Péterfalvi, G. Burkard, and J. R. Petta, High-resolution valley spectroscopy of Si quantum dots, *Phys. Rev. Lett.* **119**, 176803 (2017).
- [35] R. Ferdous, E. Kawakami, P. Scarlino, M. P. Nowak, D. Ward, D. Savage, M. Lagally, S. Coppersmith, M. Friesen, M. A. Eriksson, *et al.*, Valley dependent anisotropic spin splitting in silicon quantum dots, *npj Quantum Information* **4**, 26 (2018).
- [36] X. Mi, S. Kohler, and J. R. Petta, Landau-Zener interferometry of valley-orbit states in Si/SiGe double quantum dots, *Phys. Rev. B* **98**, 161404(R) (2018).
- [37] S. F. Neyens, R. H. Foote, B. Thorgrimsson, T. J. Knapp, T. McJunkin, L. M. K. Vandersypen, P. Amin, N. K. Thomas, J. S. Clarke, D. E. Savage, M. G. Lagally, M. Friesen, S. N. Coppersmith, and M. A. Eriksson, The critical role of substrate disorder in valley splitting in Si quantum wells, *Appl. Phys. Lett.* **112**, 243107 (2018).
- [38] F. Borjans, D. M. Zajac, T. M. Hazard, and J. R. Petta, Single-spin relaxation in a synthetic spin-orbit field, *Phys. Rev. Applied* **11**, 044063 (2019).
- [39] S. W. Oh, A. O. Denisov, P. Chen, and J. R. Petta, Cryogen-free scanning gate microscope for the characterization of Si/Si<sub>0.7</sub>Ge<sub>0.3</sub> quantum devices at milli-kelvin temperatures, *AIP Adv.* **11**, 125122 (2021).
- [40] B. Paquelet Wuetz, M. P. Losert, S. Koelling, L. E. Stehouwer, A.-M. J. Zwerver, S. G. Philips, M. T. Madzik, X. Xue, G. Zheng, M. Lodari, *et al.*, Atomic fluctuations lifting the energy degeneracy in Si/SiGe quantum dots, *Nature Communications* **13**, 7730 (2022).
- [41] M. P. Losert, M. A. Eriksson, R. Joynt, R. Rahman, G. Scappucci, S. N. Coppersmith, and M. Friesen, Practical strategies for enhancing the valley splitting in Si/SiGe quantum wells, *Phys. Rev. B* **108**, 125405 (2023).
- [42] J. R. F. Lima and G. Burkard, Interface and electromagnetic effects in the valley splitting of Si quantum dots, *Mater. Quantum. Technol.* **3**, 025004 (2023).
- [43] L. F. Peña, J. C. Koepke, J. H. Dycus, A. Mounce, A. D. Baczewski, N. T. Jacobson, and E. Bussmann, Utilizing multimodal microscopy to reconstruct Si/SiGe interfacial atomic disorder and infer its impacts on qubit variability (2023), arXiv:2306.15646 [cond-mat.mtrl-sci].
- [44] T. McJunkin, B. Harpt, Y. Feng, M. P. Losert, R. Rahman, J. Dodson, M. Wolfe, D. Savage, M. Lagally, S. Coppersmith, *et al.*, SiGe quantum wells with oscillating ge concentrations for quantum dot qubits, *Nature Communications* **13**, 7777 (2022).
- [45] J. R. F. Lima and G. Burkard, Valley splitting depending on the size and location of a silicon quantum dot (2023), arXiv:2310.17393 [cond-mat.mes-hall].
- [46] M. Volmer, T. Struck, A. Sala, B. Chen, M. Oberländer, T. Offermann, R. Xue, L. Visser, J.-S. Tu, S. Trellenkamp, Łukasz Cywiński, H. Bluhm, and L. R. Schreiber, Mapping of valley-splitting by conveyor-mode spin-coherent electron shuttling (2023), arXiv:2312.17694 [quant-ph].
- [47] J. P. Dodson, H. E. Ercan, J. Corrigan, M. P. Losert, N. Holman, T. McJunkin, L. F. Edge, M. Friesen, S. N. Coppersmith, and M. A. Eriksson, How valley-orbit states in silicon quantum dots probe quantum well interfaces, *Phys. Rev. Lett.* **128**, 146802 (2022).
- [48] X. Zhao and X. Hu, Coherent electron transport in silicon quantum dots (2018), arXiv:1803.00749 [cond-mat.mes-hall].
- [49] F. Ginzel, A. R. Mills, J. R. Petta, and G. Burkard, Spin shuttling in a silicon double quantum dot, *Physical Review B* **102**, 195418 (2020).
- [50] B. Buonacorsi, B. Shaw, and J. Baugh, Simulated coherent electron shuttling in silicon quantum dots, *Physical Review B* **102**, 125406 (2020).
- [51] X. Li, E. Barnes, J. P. Kestner, and S. D. Sarma, Intrinsic errors in transporting a single-spin qubit through a double quantum dot, *Physical Review A* **96**, 012309 (2017).
- [52] R. Ruskov, M. Veldhorst, A. S. Dzurak, and C. Tahan, Electron g-factor of valley states in realistic silicon quantum dots, *Physical Review B* **98**, 245424 (2018).
- [53] E. Ungersboeck, S. Dhar, G. Karlowatz, V. Sverdlov, H. Kosina, and S. Selberherr, The effect of general strain on the band structure and electron mobility of silicon, *IEEE Transactions on Electron Devices* **54**, 2183 (2007).
- [54] V. Sverdlov and S. Selberherr, Electron subband structure and controlled valley splitting in silicon thin-body SOI FETs: Two-band k-p theory and beyond, *Solid-State Electronics* **52**, 1861 (2008), selected Papers from the EU-ROSIO '08 Conference.
- [55] C. Adelsberger, S. Bosco, J. Klinovaja, and D. Loss, Valley-free silicon fins by shear strain (2023), arXiv:2308.13448 [cond-mat.mes-hall].
- [56] B. D. Woods, H. Soomro, E. S. Joseph, C. C. D. Frink, R. Joynt, M. A. Eriksson, and M. Friesen, Coupling conduction-band valleys in modulated SiGe heterostructures via shear strain (2023), arXiv:2310.18879 [cond-mat.mes-hall].
- [57] B. D. Woods, M. A. Eriksson, R. Joynt, and M. Friesen, Spin-orbit enhancement in Si/SiGe heterostructures with oscillating Ge concentration, *Phys. Rev. B* **107**, 035418 (2023).
- [58] J. Y. Huang, R. Y. Su, W. H. Lim, M. Feng, B. van Straaten, B. Severin, W. Gilbert, N. Dumoulin Stuyck, T. Tantt, S. Serrano, J. D. Cifuentes, I. Hansen, A. E. Seedhouse, E. Vahapoglu, R. C. C. Leon, N. V. Abrosimov, H.-J. Pohl, M. L. W. Thewalt, F. E. Hudson, C. C. Escott, N. Ares, S. D. Bartlett, A. Morello, A. Saraiva, A. Laucht, A. S. Dzurak, and C. H. Yang, High-fidelity spin qubit operation and algorithmic initialization above 1 k, *Nature* **627**, 772 (2024).
- [59] N. E. Penthorn, J. S. Schoenfeld, L. F. Edge, and H. Jiang, Direct measurement of electron intervalley relaxation in a Si/Si-Ge quantum dot, *Physical Review Applied* **14**, 054015 (2020).
- [60] C. Yang, A. Rossi, R. Ruskov, N. Lai, F. Mohiyaddin, S. Lee, C. Tahan, G. Klimeck, A. Morello, and A. Dzurak, Spin-valley lifetimes in a silicon quantum dot with tunable valley splitting, *Nature Communications* **4**, 2069

- (2013).
- [61] C. J. Wood and J. M. Gambetta, Quantification and characterization of leakage errors, *Physical Review A* **97**, 032306 (2018).
- [62] J. D. Teske, P. Cerfontaine, and H. Bluhm, qopt: An experiment-oriented software package for qubit simulation and quantum optimal control, *Physical Review Applied* **17**, 034036 (2022).
- [63] J. Yoneda, K. Takeda, T. Otsuka, T. Nakajima, M. R. Delbecq, G. Allison, T. Honda, T. Kodera, S. Oda, Y. Hoshi, *et al.*, A quantum-dot spin qubit with coherence limited by charge noise and fidelity higher than 99.9%, *Nature Nanotechnology* **13**, 102 (2018).
- [64] T. Struck, A. Hollmann, F. Schauer, O. Fedorets, A. Schmidbauer, K. Sawano, H. Riemann, N. V. Abrosimov, Ł. Cywiński, D. Bougeard, *et al.*, Low-frequency spin qubit energy splitting noise in highly purified  $^{28}\text{Si}/\text{SiGe}$ , *npj Quantum Information* **6**, 40 (2020).
- [65] N. V. Vitanov, Transition times in the Landau-Zener model, *Physical Review A* **59**, 988 (1999).
- [66] K. Mullen, E. Ben-Jacob, Y. Gefen, and Z. Schuss, Time of zener tunneling, *Phys. Rev. Lett.* **62**, 2543 (1989).
- [67] F. Schaffler, D. Tobben, H. J. Herzog, G. Abstreiter, and B. Hollander, High-electron-mobility Si/SiGe heterostructures: influence of the relaxed SiGe buffer layer, *Semicond Sci Tech* **7**, 260 (1992).
- [68] S. Müller and L. Schüler, GeoStat-Framework/GSTools: v1.5.0 ‘Nifty Neon’ (2023).
- [69] M. Friesen, S. Chutia, C. Tahan, and S. N. Coppersmith, Valley splitting theory of SiGe/Si/SiGe quantum wells, *Phys. Rev. B* **75**, 115318 (2007).
- [70] J. K. Bloomfield, S. H. P. Face, A. H. Guth, S. Kalia, C. Lam, and Z. Moss, Number density of peaks in a chi-squared field (2016), arXiv:1612.03890 [math-ph].
- [71] J. M. Bardeen, J. R. Bond, N. Kaiser, and A. S. Szalay, The Statistics of Peaks of Gaussian Random Fields, *Astrophys. J.* **304**, 15 (1986).